

Compact dust-obscured star-formation and the origin of the galaxy bimodality

Maxime Tarrasse¹, Carlos Gómez-Guijarro¹, David Elbaz¹, Benjamin Magnelli¹, Mark Dickinson², Aurélien Henry³, Maximilien Franco^{1,4}, Yipeng Lyu¹, Jean-Baptiste Billand¹, Rachana Bhatawdekar⁵, Yingjie Cheng⁶, Adriano Fontana⁷, Steven L. Finkelstein⁴, Giovanni Gandolfi^{8,9}, Nimish Hathi¹⁰, Michaela Hirschmann^{11,12}, Benne W. Holwerda¹³, Anton M. Koekemoer¹⁰, Ray A. Lucas¹⁰, Lise-Marie Seillé¹⁴, Stephen Wilkins^{15,16}, and L. Y. Aaron Yung¹⁰

(Affiliations can be found after the references)

October 2024

ABSTRACT

Context. The combined capabilities of the *James Webb* Space Telescope/Near Infrared Camera (NIRCam) and the *Hubble* Space Telescope/Advanced Camera for Surveys (ACS) instruments provide high angular resolution imaging from UV-to-NIR wavelengths, offering unprecedented insight into the inner structure of star-forming galaxies (SFGs) even when they are shrouded in dust. In particular, a population of highly attenuated and massive red SFGs (RedSFGs) at $z \sim 4$, can now be spatially resolved and studied in the rest-frame optical/near-infrared (NIR). These RedSFGs represent a crucial population for unraveling the mechanisms driving the transition from vigorous star formation to quiescence, as they probably are the progenitors of the massive and passive galaxies already in place at cosmic noon.

Aims. We assembled a mass-complete sample of massive galaxies at $z = 3 - 4$ in order to study and compare the stellar mass, star-formation rate (SFR), dust attenuation and age spatial distributions of RedSFGs with those of quiescent galaxies (QGs) and more typical blue SFGs (BlueSFGs). **Methods.** We performed injection-recovery of galaxies with various profiles in the CEERS images to build a mass-complete sample of 188 galaxies with $\log(M_*/M_\odot) > 9.6$ that we classified into BlueSFGs, RedSFGs and QGs. We performed resolved spectral energy distribution (SED)-fitting on the UV-to-NIR data to compute and compare radial profiles of these three populations.

Results. The RedSFGs fraction is systematically higher than the one of QGs and both increase with stellar mass. Together, they account for more than 50% of galaxies with $\log(M_*/M_\odot) > 10.4$ at this redshift. This transition mass corresponds to the $\log(M_*/M_\odot) \sim 10.4$ threshold often referred to as the "critical mass" delineating the bimodality between BlueSFGs and QGs in the local Universe. We find that RedSFGs and QGs present similar stellar surface density profiles and that RedSFGs manifest a dust attenuation concentration significantly higher than that of BlueSFGs at all masses. While this explains the systematically higher dust attenuation of these galaxies on global scales, it also indicates that to become quiescent, a BlueSFG must transit through a major compaction phase once it has become sufficiently massive. We conclude that RedSFGs are probably observed during this compaction phase building a massive bulb in situ.

Conclusions. There is a bimodality between extended BlueSFGs and compact and strongly attenuated RedSFGs that have undergone a phase of major gas compaction. There is evidence that this early-stage separation is at the origin of the local bimodality between BlueSFGs and QGs, which we refer to as a "primeval bimodality".

Key words. galaxies: evolution – galaxies: star formation – galaxies: structure – infrared: galaxies

1. Introduction

Over the past few decades, our understanding of galaxy evolution has been greatly enhanced by multi-wavelength observations. In particular, the identification of a star-formation main-sequence (MS; Daddi et al. 2007; Elbaz et al. 2007; Noeske et al. 2007; Schreiber et al. 2015) at least up to $z = 6$ (Popesso et al. 2023; Calabro et al. 2024), with hints of its presence up to $z = 9$ (Ciesla et al. 2024), suggests that the bulk of present-day stars formed through a secular process rather than through a series of bursts. Nevertheless, QGs do not follow this correlation and are located below the MS, indicating a suppressed star-formation for this population. This change in specific star formation ($sSFR \equiv SFR/M_*$) is not fully understood and correspond to the clear color bimodality observed between QGs and SFGs, these later having typically blue continuum-dominated spectra produced by massive young stars, while the former have redder spectra, dominated by the emission of older, less massive stars (Baldry et al. (2004); Williams et al. (2009); Patel et al. (2012)). This color bimodality also seems to be accompanied by a mor-

phological bimodality linked to their morphological evolution (Lee et al. 2013; Osborne et al. 2020; Liu et al. 2019), with SFGs exhibiting disk structures (Sérsic index, $n \sim 1$), whereas QGs have more compact morphologies (Sérsic index, $n \sim 4$) (van der Wel et al. 2014; Ward et al. 2024). This morphological and color bimodality has been shown to arise at high mass (Wuyts et al. 2011; Huertas-Company et al. 2024), suggesting that the rise of this bimodality is more of a mass-driven process rather than being SFR- or morphology-driven process (Conselice et al. 2024). Additionally, the number density of QGs was shown to dominate the one of SFGs for $10 < \log(M_*/M_\odot) < 11$ galaxies for redshifts lower than $z = 2$ (Brammer et al. 2011; Muzzin et al. 2013; Weaver et al. 2023). As this redshift defines the peak of the star formation rate density (SFRD) and coincides with a significant fraction of QGs in place at cosmic noon, it implies that this bimodality between SFGs and QGs arises early in the history of the Universe. Therefore, studying the possible progenitors of massive QGs already in place at $z \sim 2$ is essential to our understanding of how SFGs transit to quiescence.

In this context, the combined capabilities of the *Spitzer* Space Telescope (*Spitzer*) and the Atacama Large Millimeter-/submillimeter Array (ALMA), has shed light on a population of galaxies extremely faint from the rest-frame UV up to the optical, making them undetectable even in the reddest and deepest images of the *Hubble* Space Telescope (HST) (Caputi et al. 2012; Wang et al. 2016; Franco et al. 2018; Wang et al. 2019; Yamaguchi et al. 2019; Williams et al. 2019). This population was seen as a serious candidate to be the progenitor of the massive QG population observed at high redshifts (Carnall et al. 2023a) given their significant contribution to the high-mass end ($\log(M_*/M_\odot) > 10.3$) of the cosmic SFRD and stellar mass density (SMD) at $3 < z < 6$, and their halo mass ($\sim 10.13 h^{-1} M_\odot$ at $z = 4$) that aligns with this hypothesis (Wang et al. 2019; Gruppioni et al. 2020). To detect this population, Wang et al. (2019) used the *H*-dropout selection technique, which consists of searching for sources with very weak detection in the *H*-band (typically $H > 27$ mag) and bright detection in the *Spitzer*/IRAC [4.5 μ m]-band (typically $[4.5] < 24$). Because of these observed properties, this selection resulted in a population of $z > 3$ massive SFGs, heavily obscured by dust. These galaxies are referred to as "HST-dark", "*H*-dropouts" or "optically-dark" galaxies.

To fill the gap between Lyman break galaxies (LBGs; Giavalisco et al. 2004a; de Barros et al. 2014; Arrabal Haro et al. 2020) and *H*-dropouts at $3 < z < 6$, Xiao et al. (2023b) extended the HST-dark population to a wider selection ($H > 26.5$ and $[4.5] < 24$) that provides a more complete view of SFRD at these redshifts by considering galaxies that are less extreme in terms of dust attenuation and stellar mass. The first studies of this so-called optically-faint galaxy (OFG) population using photometric and ALMA data have located it at the high-mass end of the MS ($\log(M_*/M_\odot) > 10$) with particularly high dust attenuation ($A_V > 2$), high star formation efficiency (SFE) and low gas fraction, suggesting a highly efficient conversion of cold gas into stars in these systems (Alcalde Pampliega et al. 2019; Gómez-Guijarro et al. 2022; Xiao et al. 2023b; Gómez-Guijarro et al. 2023; Xiao et al. 2023a). Nevertheless, *Spitzer*'s low angular resolution in the NIR have not permitted a thorough morphological study of this population, and of galaxies at these redshifts in general.

With the launch of JWST, astronomers now have access to unprecedentedly deep and high angular resolution NIR imaging at wavelengths longer than 2 μ m, enabling them to spatially resolve the stellar structures of galaxies across cosmic time (Gardner et al. 2006, 2023). While the definition of this population of red, dust obscured star-forming population, heavily depend on the color criteria used, first studies using JWST NIR observations have confirmed their high contribution to the high-mass end of the SFRD ($\sim 3.2 \times 10^{-3} M_\odot \text{ yr}^{-1} \text{ Mpc}^{-3}$) from $z = 3$ up to $z = 7$ (Barrufet et al. 2023) and total SMD, the latter having been found to be underestimated in the pre-JWST area by $\sim 20\%$ for $3 < z < 4$ and up to $\sim 40\%$ for $6 < z < 8$ (Gotumukkala et al. 2024; Weibel et al. 2024). Additionally, spectroscopic and optical-to-mid-IR observations of some of these sources have confirmed their high redshift, massive and dusty properties, while discussing the potential triality of their nature namely star-forming ($\sim 70\%$), quiescent ($\sim 20\%$), and potentially AGN or young starbursts ($\sim 10\%$) at $2 < z < 7$ (Pérez-González et al. 2023; Barrufet et al. 2024). A few papers have used the resolving power in the NIR to study the internal structures of these galaxies, highlighting their stellar and dust concentrated profiles (Pérez-González et al. 2023; Nelson et al. 2023; Gómez-Guijarro et al. 2023; Smail et al. 2023; Sun et al. 2024). Although these new studies seem to link this population even more strongly to

the QGs, their spatially resolved properties are still poorly understood as they only focus on small samples and suffer from completeness bias. We therefore lack morphological evidence that this population corresponds to a key transition phase between SFGs and QGs.

In this work we study the spatial distribution of different physical quantities for a mass-complete sample at $3 < z < 4$ using a resolved SED-fitting procedure. We compute and compare the radial profiles of color-selected QGs, typical blue SFGs (hereafter referred as BlueSFGs) and red SFGs (RedSFGs) which include, but are not limited to, OFGs (see selection in Fig 5). This way we aim to decipher the nature and potential role of the RedSFG population in the morphological transition from BlueSFGs to QGs.

This paper is organized as follows: In Sect. 2, we introduce our data, which includes JWST/NIRCam and HST/ACS observations from the CEERS field, and the associated catalog. We also present our SED fitting analysis, which we use for both resolved and unresolved studies, and take particular care to explain the choice of attenuation law for this work. Sect. 3 is dedicated to the method used to assemble a mass-complete sample of BlueSFGs, RedSFGs and QGs. In Sect. 4, we analyze the results of this resolved SED fitting method and in particular compare the radial profiles of the physical properties of BlueSFGs, RedSFGs, and QGs. We discuss in Sect. 5 how these results highlight the role of the RedSFG population in galaxy evolution by integrating our results into the broader framework of galaxy evolution. Finally, Sect. 6 summarizes our findings.

Throughout this work, we adopt a flat cosmology with $[\Omega_\Lambda, \Omega_M] = [0.7, 0.3]$ and set the Hubble constant to $H_0 = 70 \text{ km.s}^{-1}$. We also quote all magnitudes in the AB system (Oke & Gunn 1983).

2. Observations and Data Description

2.1. CEERS data

In this study, we used imaging data obtained by the JWST/NIRCam instrument as part of the Cosmic Evolution Early Released Science (CEERS) survey (Finkelstein et al. 2017). It has been conducted in the Extended Groth Strip (EGS) field (Finkelstein et al. 2022) and contains 10 pointings, covering a total area of 97 square arcminutes. CEERS provided the first deep extragalactic survey with JWST in seven NIRCam filters (*F115W*, *F150W*, *F200W*, *F277W*, *F356W*, *F410M*, and *F444W*) with a median 5σ point source depth of 29.20, 29.01, 29.16, 29.15, 29.15, 28.32, and 28.56, respectively. Additionally, we used the *F606W* and *F814W* optical-bands from HST observations with the ACS/WFC instrument, having a 5σ point source depth of 28.73 and 28.50, respectively (Davis et al. 2007; Finkelstein et al. 2024).

The JWST/NIRCam data have been reduced following Bagley et al. (2023) and the produced images were pixel aligned to the HST/ACS images of the Cosmic Assembly Near-infrared Deep Extragalactic Legacy Survey (CANDELS; Koekoer et al. 2011; Grogin et al. 2011). In brief, pointings from June 2022 were processed using the JWST Calibration pipeline v1.7.2 and CRDS pmap 0989, while those from December 2022 were processed using the JWST Calibration pipeline v1.8.5 and CRDS pmap 1023. Then, a customized pipeline developed by the CEERS team incorporating procedures such as $1/f$ noise subtraction and artifact removal was applied to all pointings. Finally, mosaics were aligned using astrometry data from Gaia-

EDR3 (Gaia Collaboration et al. 2021), with a pixel scale of 0.03 arcsec/pixel, and background subtracted.

2.2. Catalog

We used the photometric catalog built by Gómez-Guijarro et al. (2023) that contains our nine HST/JWST bands of interest (*F*606W, *F*814W, *F*115W, *F*150W, *F*200W, *F*277W, *F*356W, *F*410M, *F*444W) together with the CFHT/MegaCam observations imaging in the EGS field in the u^* , g' , r' , i' , and z' -bands. This cataloging analysis provided segmentation maps, fluxes and flux uncertainties for each source across the 10 CEERS pointings in both the two HST and seven JWST bands used in this study. To briefly summarize the construction of this catalog, they employed SExtractor (Bertin & Arnouts 1996) following a methodology similar to the one performed in the CANDELS catalog within the EGS field (Stefanon et al. 2017) but with the *F*444W-band serving as the detection image. Fluxes and their respective errors for each source were measured using Kron elliptical apertures on images that were PSF-matched to the 0.16" FWHM angular resolution of the *F*444W-band images. A series of corrections were then applied to address aperture corrections and PSF effects.

From this photometric catalog, Gómez-Guijarro et al. (2023) estimated the photometric redshift for each source from a SED fitting procedure with the 18 fluxes and corresponding uncertainties from their catalog as input of the EAZY-py code, an updated Python version of the code EAZY (Brammer et al. 2008). To ensure the best photometric redshift determination possible, they employed a set of 13 Flexible stellar population synthesis (FSPS; Conroy & Gunn 2010) templates (corr_sfhz_13; Kokorev et al. 2022) allowing the SED code to span various star-formation histories (SFH), ages and dust attenuation while including the contributions of emission lines to the spectra. When available in the spectroscopic redshift catalog of Stefanon et al. (2017) or in the MOSDEF survey of the EGS field (Kriek et al. 2015), photometric redshifts were replaced by spectroscopic redshifts. Here we focus our analysis on the $3 < z < 4$ redshift range because the number distribution of RedSFGs (see selection criteria in Sect. 3.3) peaks there (~60%) in our catalog. To ensure a good mass determination, we restricted our analysis to galaxies with photometric redshifts $3 < z < 4$ to be significantly detected ($> 5\sigma$) in the *F*444W and *F*356W-bands. We also carried out an analysis about photometric redshift uncertainties using different SED-fitting codes to verify the quality of our EAZY-based photometric redshifts. To this end, SED fitting of the 1755 galaxies was performed with Beagle (Chevallard & Charlot 2016), Cigale (Boquien et al. 2019), Lephare (Arnouts et al. 1999; Ilbert et al. 2006) and HyperZ (Bolzonella et al. 2000) and compared with the redshifts determined by EAZY. In the end, we imposed a relative error cut in the redshift determination such that $|z_{\text{EAZY}} - z_{\text{median}}|/z_{\text{EAZY}} < 20\%$. In our redshift range of interest ($3 < z < 4$) and above our stellar mass limit (see Sect. 3.2), 21 out of 237 galaxies (~9%) are excluded by this criterion, with only one that would have been identified as RedSFGs in Sect. 3.3. In what follows, we adopt the photometric redshifts from EAZY.

2.3. AGN

We also identified and removed galaxies with potential AGN contamination from our sample, as this population could distort the stellar properties of the resolved SED-fitting and, con-

sequently, its interpretation. When looking for the signature of AGN with photometric data, we need to use different color criteria, as AGN can be of different natures and therefore detectable at different wavelengths. To seek for unobscured AGN, we cross-matched our sample to the AEGIS-XD catalog of Luo et al. (2016) and computed X-ray luminosities in the rest-frame 2–10 keV band using the 0.5–10 keV flux k -corrected using a power-law X-ray spectrum with a spectral index of $\Gamma = 1.4$ similarly to Kocevski et al. (2023a). We then imposed the $\log(L_X/L_\odot) > 42.5$ threshold commonly used to differentiate unobscured AGN from star-forming galaxies (e.g. Luo et al. 2016) and removed 8 out of 208 galaxies. For obscured AGN, we searched for infrared AGN contribution in the FIR catalog of Henry et al., (in preparation) that uses the super-deblending technique from Liu et al. (2018); Jin et al. (2018). We used the rest-frame UV-to-NIR fluxes from both our HST/ACS and JWST/NIRCam data and added the super-deblended photometry from Spitzer/IRAC 5.8, 8 μm and MIPS 24 μm , Herschel/PACS 100, 160 μm and SPIRE 250, 350, 500 μm and JCMT/SCUBA2 450, 850 μm . We performed a SED-fit using the Code Investigating GALaxy Emission (Cigale; Boquien et al. 2019) and fit the AGN contribution to the SED of galaxies with $S/N > 3$ in the 8 μm and 24 μm -bands. By defining the AGN fraction f_{AGN} as the AGN contribution to the total IR luminosity $L_{\text{IR}}^{\text{AGN}} = f_{\text{AGN}} \times L_{\text{IR}}^{\text{tot}}$, we removed 4 out of 208 galaxies from our sample that have $f_{\text{AGN}} > 0.2$. Finally, as the accretion disk and the jets of AGN produce synchrotron emission, radio detections have been historically used to detect heavily obscured AGN. However, due to synchrotron emission from supernova remnants, SFGs can also be bright in the radio band, and this radiation correlates with their rest-frame 42 to 122 μm FIR emission from (Helou et al. 1985; Yun et al. 2001; Magnelli et al. 2015) and more generally the rest-frame 8 to 1000 μm infrared emission (Bell 2003; Delhaize et al. 2017). Therefore, a commonly used method is to identify AGN as galaxies that deviate by more than 3σ from the correlation followed by SFGs. Following Delvecchio et al. (2017), this is achieved by imposing a lower limit on the radio excess parameter such as :

$$r = \log\left(\frac{L_{1.4\text{GHz}}[\text{W.Hz}^{-1}]}{\text{SFR}_{\text{IR}}[\text{M}_\odot.\text{yr}^{-1}]}\right) > 22 (1+z)^{0.013} \quad (1)$$

where $L_{1.4\text{GHz}}$ is the 1.4 GHz rest-frame luminosity and SFR_{IR} is computed from the integrated 8–1000 μm infrared luminosities. Here, we use the super-deblended FIR catalog of Henry et al., (in preparation) that provides SFR_{IR} from FIR+submm (observed 100 μm to 1.1 mm) SED fit and $L_{1.4\text{GHz}}$ using the 3 GHz flux density following Wang et al. (2023). We removed 1 out of 204 additional source following this method. We also report the presence of five sources with extremely low luminosity given their stellar mass of $\log(M_*/M_\odot) \sim 10$ in our mass-complete sample. Visual inspection of these sources revealed their extremely small size while showing an extremely high dust attenuation ($A_{\text{v,median}}^{\text{ISM}} \sim 4$) and SED expected for "little red dots" (Labbe et al. 2023; Kokorev et al. 2024). Indeed, three of them are selected as LRD by the SED's continuum slope fit from Kocevski et al. (2024) with two being spectroscopically confirmed $z_{\text{spec}} = 5.08$ and $z_{\text{spec}} = 5.62$ highly obscured AGN showing broad emission lines with NIRSpc (CEERS 5760 in Kocevski et al. (2024) and CEERS 82815 in Kocevski et al. (2023b)). We therefore decided to exclude them from this analysis. In the end, we removed 18 potential AGN contaminants from the mass-complete sample of 216 galaxies with secure photometric redshifts (see Sect. 2.2).

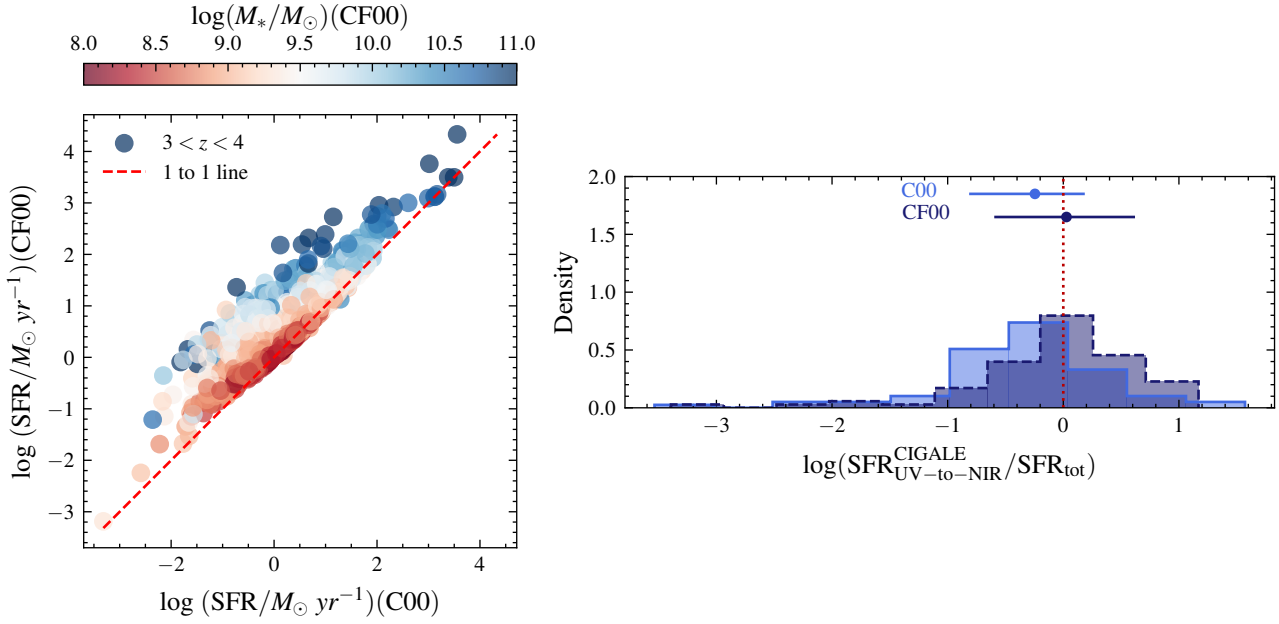


Fig. 1: *Left panel* : measurement comparisons of SFR obtained by SED-fitting with the CF00 and C00 attenuation law for the 1202 galaxies at $3 < z < 4$ taken from the Gómez-Guijarro et al. (2023) photometric catalog with cleaned photometric redshifts and without potential AGN contaminants and poorly fitted galaxies. *Right panel* : Comparative histograms of the SFR ratio between the UV-to-NIR SFR obtained by SED-fitting with the CF00 (dark blue) and C00 (light blue) attenuation law and the $\text{SFR}_{\text{tot}} = \text{SFR}_{\text{UV}} + \text{SFR}_{\text{IR}}$. UV-to-NIR data are from JADES and SFR_{tot} from the GOODS-ALMA 2.0 catalog. For each distribution, the median value (filled circle) along with its associated 16% and 84% percentiles (segments) are displayed. The red dotted vertical line indicates the benchmark such that 100% of the total SFR is retrieved by the UV-to-NIR SED-fit.

2.4. Mass, star formation rate and attenuation law

Galaxies in our catalogue are then fitted with Cigale. To compute the stellar component of our SED models, we assumed a delayed, exponentially declining star-formation history (SFH) such as $\text{SFR} \propto \frac{1}{\tau^2} \times \exp(-t/\tau)$ where τ defines the time at which the SFR peaks, and used the (Bruzual & Charlot 2003) (BC03) stellar population synthesis model together with a Chabrier (2003) initial mass function (IMF) and the Charlot & Fall (2000) (CF00) dust attenuation law (see below for more tests on that matter). To decide whether or not letting metallicity free during the fit, we investigated the constraining power of our UV-to-NIR data on this parameter by using the mock analysis from Cigale similarly to Seillé et al. (2022). Briefly, Cigale uses the best-fit model fluxes and their associated observed photometric errors to run with the same configuration grid but with flux values randomly chosen within a Gaussian distribution centred of the best-fit value and the photometric error as a standard deviation. Cigale then compares the result from the initial run with this run based on mock SED. Based on this analysis, we concluded that metallicity was not constrained with our data. Therefore, we decided to fix the metallicity to solar ($Z = 0.2$), as it has been shown to be a good assumption for massive $\log(M_*/M_\odot) > 9.6$ galaxies, according to the mass-metallicity relation at this redshift (Ma et al. 2016). We also tested the contribution of a nebular continuum with emission lines on the properties derived from our mass-complete sample defined in Sect. 3.2. We fitted galaxies with and without the nebular module and found no notable effects on the SFR, A_V and mass-weighted age. Nevertheless, we noticed a slight effect on stellar mass, with the inclusion of the nebular continuum overestimating the mass of ~ 0.1 dex on average compared to fit with the nebular component for $\log(M_*/M_\odot) < 10$ galaxies, in agreement with Yuan et al.

(2019). Based on these results, and since our main results are drawn from the most massive $\log(M_*/M_\odot) > 10$ galaxies of our mass-complete sample, the choice of including nebular emission does not impact the results. Then, we decided to not include the nebular emission while fitting. To ensure reasonable parameter estimates, we finally excluded galaxies with bad fit, defined as galaxies with $\chi^2_{\text{reduced}} > 1.68$ as this upper limit corresponds to a significance level of 10% for data with 8 degrees of freedom (9-1 photometric bands). We removed 10 out of 198 additional galaxies based of this criteria in our mass-complete sample derived in Sect. 3.2.

Since we want to study very dusty galaxies, the choice of an attenuation law is crucial. In fact, different laws can lead to different mass and SFR determinations if the dust emission is not considered, which is the case without FIR data (Buat et al. 2019). With Cigale we can use a Calzetti et al. (2000) (C00), or a Charlot & Fall (2000) (CF00) attenuation-law. In C00, dust attenuation at a given wavelength is measured using the color excess as $A_\lambda = E(B-V)_{\text{stars}} k_\lambda$ where k_λ defines the reddening curve and $k_V = \frac{A_V}{E(B-V)_{\text{stars}}} = R_V$. On the other hand, the CF00 assumes that young (< 10 Myrs) and old stars do not undergo the same total attenuation. In this model, young stars have not yet left their birth clouds, so their light is attenuated by both the birth cloud and the ISM, whereas for old stars, their radiation is only affected by the dust in the ISM. To model these two attenuating components, CF00 considers two power-law attenuation curves, one for the birth cloud, $A_\lambda^{\text{BC}} = A_V^{\text{BC}} (\lambda/0.55)^{n^{\text{BC}}}$ and one for the ISM, $A_\lambda^{\text{ISM}} = A_V^{\text{ISM}} (\lambda/0.55)^{n^{\text{ISM}}}$ with the ratio between the attenuation of the two components controlled by $\mu = \frac{A_V^{\text{ISM}}}{(A_V^{\text{BC}} + A_V^{\text{ISM}})}$. Because the power-law indices and μ are not constrained by UV-to-NIR data (Buat et al. 2012, 2019; Seillé et al. 2022), we opted and then

Table 1: Cigale model parameters

Module	Parameter	Symbol	Values
Star formation history	e -folding timescale of the delayed SFH for the main population	τ_{main}	1-30 Gyr
<i>sfhdelayed</i>	age of the main stellar population	t_{main}	0.1-3 Gyr
Simple stellar population	Initial mass function		Chabrier2003
<i>Bruzual and Charlot 2003</i>	Metallicity	Z_{\odot}	0.02
Dust attenuation	V-band attenuation in the ISM	A_V^{ISM}	0-5
<i>Charlot Fall 2000</i>	$\frac{A_V^{\text{ISM}}}{A_V^{\text{BC}} + A_V^{\text{ISM}}}$	μ	0.3
	Power law slope of dust attenuation in the birth cloud	n^{BC}	-0.7
	Power law slope of dust attenuation in the interstellar medium	n^{ISM}	-0.7

tested the initial CF00 formulation with $n^{\text{ISM}} = n^{\text{BC}} = -0.7$ and $\mu = 0.3$.

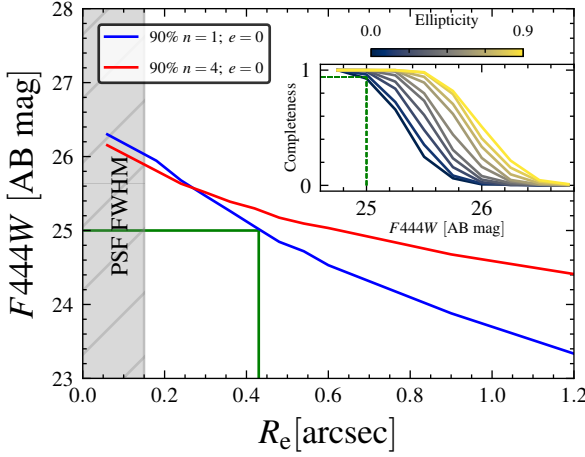


Fig. 2: Determination of the $F444W$ limiting magnitude. The dependence of the 90% limiting magnitude on circularized effective radii from $0''.06$ to $1''.2$ is shown for an exponential profile ($n = 1$, blue solid line) and a de Vaucouleurs profile ($n = 4$, red solid line), both with null ellipticity ($e = 0$). In the top right-hand corner, we show the completeness curves for a Sérsic profile $n = 1$ with size $R_e = 0''.42$ and variable ellipticity and the projection of the 90% completeness on the $e = 0$ curve that is the most restrictive one. The grey shaded region depicts the FWHM size of the $F444W$ -band. The green solid lines defines the $F444W = 25$ limiting magnitude as the projection on the most restrictive, while realistic, galaxy size ($R_e = 0''.42$) and ellipticity ($e = 0$) at $z = 3.5$.

Firstly, we compared the SFRs inferred by Cigale while using the C00 or CF00 attenuation law on all galaxies of our catalog with $3 < z < 4$. As the left panel of Fig. 1 suggests, C00 and CF00 SFRs are similar for galaxies with low stellar mass ($\log(M_*/M_{\odot}) < 9.5$) at these redshifts, while high-mass sources present significantly higher SFRs when using CF00 attenuation law. We therefore investigated the accuracy of the inferred SFR of both attenuation laws for massive galaxies, taking advantage from the GOODS-ALMA 2.0 catalog (Gómez-Guijarro et al. 2022) that contains massive ALMA-detected sources in the Great Observatories Origins Deep Survey South field (GOODS-South; Dickinson et al. 2003; Giavalisco et al. 2004b). This catalog provides total SFRs that take into account unobscured and obscured SFRs such that $\text{SFR}_{\text{tot}} = \text{SFR}_{\text{UV}} + \text{SFR}_{\text{IR}}$. In this catalog, SFR_{IR} was obtained by using mid-IR to mm SED-fit of galaxies detected with a peaked significance

level of $> 5\sigma$. They derived the total L_{IR} by integrating the best-fit curve between rest frame 8 and $1000 \mu\text{m}$, and subtracted a potential AGN contribution to IR emission. The deduced L_{IR} therefore only takes into account star formation, and is translated into SFR_{IR} using the Kennicutt (1998) conversion. Then, we cross-matched these 88 galaxies from the GOODS-ALMA 2.0 catalog and which have $\log(M_{\text{median}}/M_{\odot}) \sim 10.77$ and $z_{\text{median}} = 2.46$ to the JWST Advanced Deep Survey (JADES; Eisenstein et al. 2023b; Bunker et al. 2024; Eisenstein et al. 2023a; D'Eugenio et al. 2024; Hainline et al. 2024; Rieke et al. 2023) catalog to obtain their UV-to-NIR data. We performed SED fits of these galaxies and compared the SFRs obtained using UV-to-NIR data with a C00 or CF00 attenuation law to the total SFRs from the GOODS-ALMA 2.0 catalog. The right panel of Fig. 1 suggests that the median SFR obtained by the CF00 law is in better agreement with the ALMA SFR, with $\Delta\log(\text{SFR}_{\text{median}}/M_{\odot}.\text{yr}^{-1}) = 1.1^{+3.9}_{-4.2}$ while the one from using the C00 law has $\Delta\log(\text{SFR}_{\text{median}}/M_{\odot}.\text{yr}^{-1}) = 0.57^{+2.7}_{-3.7}$. In view of this result, we decided to use the CF00 attenuation law. The table showing the Cigale grid used in the rest of the article (including the resolved SED-fitting) can be found in Table. 1.

3. Mass-complete sample determination and classifications

3.1. Apparent magnitude limit

The completeness of a catalog is defined as the fraction of sources in a field that are actually detected as a function of their observed magnitudes. Nevertheless, the detectability of a source not only depends on its flux but also on its surface brightness and thus its morphology. As we aimed to study a mass-complete sample of galaxies at $3 < z < 4$ in this work, we evaluated the 90% limiting magnitude in the $F444W$ detection band of our catalog for a large grid of profiles presented in Tab. 2.

We randomly injected 100 sources in each of the 10 pointings in bins of magnitudes and with various Sérsic profiles across the whole field. We ensured that the injected profiles did not overlap with pre-existing sources as determined by the SExtractor segmentation map, and we avoided placing injected sources near the edges of the pointings or in a vicinity of a bright source. On these images, we ran the detection procedure used to generate the catalog presented in Sect. 2.2 and computed the ratio $N_{\text{recovered}}/N_{\text{injected}}$ for each of the 10 fields. We subsequently calculated the mean of these values to generate the final completeness curves of the total field. The results are summarized in Fig. 2 that shows how the 90% limiting magnitude (i.e the magnitude at which 90% of the sources are recovered) is influenced by the size and brightness profile of the source. It highlights that for galaxies with sizes close to the PSF FWHM of the detection band,

Table 2: Simulations input parameters

Parameter	Values
$m_{4.4\mu\text{m}}[\text{mag}]$	20-30, step 0.25
n	1,4
$R_e[\text{arcsec}]$	0.06, 0.18, 0.24, 0.3, 0.36, 0.42, 0.48, 0.56, 0.6, 0.9, 1.2
$e = 1 - b/a$	0-0.9 step 0.1

the Sérsic index does not have a significant impact on the detection limit. Nevertheless, differences arise at $\sim 2 \times \text{FWHM}$ with higher Sérsic index (i.e., a cusper surface brightness) profiles detected down to a higher magnitude than lower Sérsic index profiles. On the upper-right corner of this figure, we display different completeness curves of sources injected with ellipticities ranging from $e = 0.9$ (highly elliptical) to $e = 0$ (perfect circle) for a fixed $n = 1$ and $R_e = 0''.42$. These choices of Sérsic index and R_e to derive our detection limit are motivated by the broad morphological study of galaxies at redshift $z > 3$ conducted in Kartaltepe et al. (2023) using JWST/CEERS data in which they extracted Sérsic index and effective radius distributions for their sample. To derive a conservative estimate of the limiting magnitude, we used the results from the injection-recovery method of sources with $n = 1$ together with the higher R_e found in Kartaltepe et al. (2023) ($3\text{kpc} = 0''.42$ at $z = 3.5$, the redshift of our study), coupled with a null ellipticity. The orthogonal projection of this galaxy size on the $n = 1$ curve with $e = 0$ is shown as green solid lines.

These results highlight that injection-recovering of only point sources will tend to artificially increase the limit in magnitude compared to extended sources, thus introducing potential bias into subsequent completeness-based analysis, which was already found in the paper of Stefanon et al. (2017). In the end, we determined a value of $m_{\text{lim},4.4\mu\text{m}} = 25$ as the most conservative estimate for the limiting magnitude in the $F444W$ -band.

3.2. Mass Completeness

In order to obtain a mass-complete sample of galaxies detected at $3 < z < 4$, the apparent limiting magnitude must be translated into a limiting mass above which we control the fraction of galaxies that could have been missed by our detection method. However, mass determination suffers from systematic uncertainties even when NIR data are available as its determination can be affected by the SED-fitting code used, the prior assumptions made to compute the stellar populations (Gawiser 2009; Lower et al. 2020; Pacifici et al. 2023; Narayanan et al. 2024) and most importantly the intrinsic variation of the SED shape of each galaxy according to its formation and evolution history and the redshift uncertainty. This in turn implies that it is impossible to simply convert the apparent magnitude limit determined in Sect. 3.1 into a limiting mass using simply a constant stellar mass-to-light ratio.

We therefore determined the 90% mass-completeness limit empirically from our catalog sample of 1202 galaxies cleaned from insecure photometric redshifts, potential AGN contaminants, and poorly fitted galaxies. To do so, we followed Schreiber et al. (2015) and exploited the relation between the rest-frame $L_{\lambda}^{\text{rest}}$ where $\lambda = 4.4/(1+z) = 1 \pm 0.1 \mu\text{m}$ in this range of redshift, and the stellar mass inferred by Cigale using the full UV-to-NIR photometry of each galaxy. As shown in Fig. 3, the mass versus light relation and its corresponding 1σ scatter vary with mass, the later ranging from ~ 0.18 dex at low

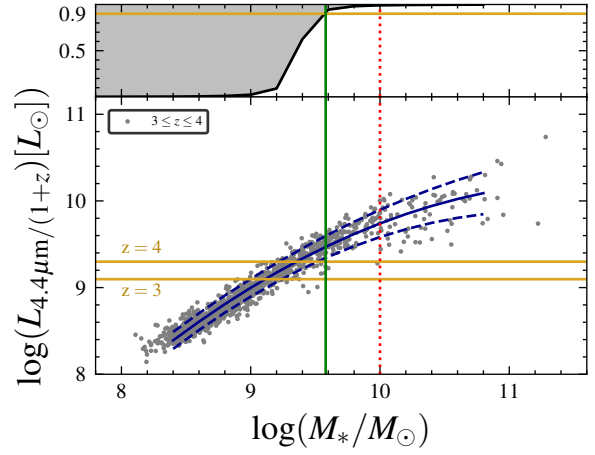


Fig. 3: *Lower panel* : Distribution in stellar mass and luminosity at rest-frame wavelength $4.4\mu\text{m}/(1+z)$ with $3 \leq z \leq 4$. The best-fit relation with its 1σ dispersion are displayed in solid and dashed blue lines, respectively. The position of the $F444W = 25$ limiting magnitudes for $z = 3$ and $z = 4$ are shown with two golden lines. *Upper panel* : Evolution of completeness with stellar mass at the $z = 4$ luminosity limit. The horizontal golden line showing the 90% completeness level. Consequently, the green vertical line defines the estimated 90% mass completeness limit. Taking into account galaxies with low mass-to-light ratios, our sample is 99% complete for this population to the right of the red dotted line.

mass (i.e., $\log(M_*/M_\odot) \sim 8.4$) to ~ 0.58 dex at high mass (i.e., $\log(M_*/M_\odot) \sim 11$). This increasing scatter is mainly due to the presence of a population of galaxies with $\log(M_*/M_\odot) > 10$ that are outliers of the main relation by showing high mass-to-light ratio. It appears that all of these galaxies that deviate by more than 1σ from the main relation are classified as RedSFGs in Sect. 3.3, therefore hinting at their highly dusty nature ($A_{\text{v,median}}^{\text{ISM}} \sim 2.2$). We incorporated the evolution of the mass-to-light ratio and its scatter in our limiting mass determination by fitting them with a second degree polynomial function. Using the best fit equations, we generated Gaussian distributions of mock galaxies in stellar mass bins and computed the fraction of galaxies that have their luminosities greater than a given limiting luminosity. Because a source with a given flux can have different deduced rest-frame luminosities depending on its redshift, to be as conservative as possible, we imposed the $z = 4$ limiting luminosity and considered our sample to be complete in mass when completeness exceeded 90%.

The final mass-complete sample comprises 188 galaxies above a limiting mass of $\log(M_{*\text{lim}}/M_\odot) = 9.6$ and is cleaned of uncertain redshifts, bad fits and AGN contaminants (see Sect. 2). We note that although this 90% completeness threshold is commonly used in the literature, the 10% of galaxies missed down to this mass limit have by definition a particularly high mass-to-light ratio and are in practical associated with RedSFGs defined in the following section. Consequently, our sample could be significantly biased against lower mass RedSFGs. To obtain a mass complete sample of RedSFGs, we therefore need to impose an even stricter completeness threshold of 99%, which is reached at $\log(M_*/M_\odot) = 10$. Above this threshold, we can consider our sample complete for BlueSFGs, RedSFGs and QGs. Between $\log(M_*/M_\odot) = 9.6$ and $\log(M_*/M_\odot) = 10$, our sample can be

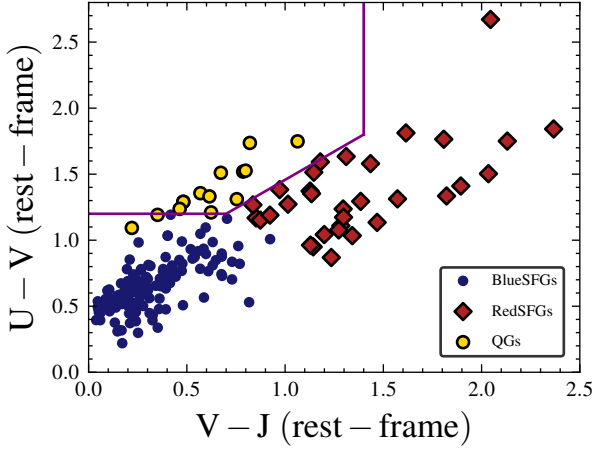


Fig. 4: Location of BlueSFGs, RedSFGs and QGs at $3 < z < 4$ in the UVJ color-color diagram, the purple line delimits the quiescent region as defined in Whitaker et al. (2011).

considered complete for QGs and BlueSFGs but incomplete for RedSFGs.

3.3. Classifications

The goal of this study is to examine the connection between BlueSFGs, RedSFGs and QGs. To achieve this, the first step was to categorize each galaxy as SFG or QG. We identified the QG population amongst our mass-complete sample of 188 galaxies by using the union of the widely used UVJ color criteria (Patel et al. 2012; Fumagalli et al. 2014; Fang et al. 2018; Valentino et al. 2020, 2023; Carnall et al. 2023b) with a criteria based on the distance below the main sequence $\Delta MS = SFR/SFR_{MS}$. Here, we used the UVJ diagram as defined by Whitaker et al. (2011):

$$\text{Quiescent} = \begin{cases} U - V > 1.2 \\ V - J < 1.4 \\ U - V > 0.88 \times (V - J) + 0.59 \end{cases}$$

and defined as quiescent, sources that enter the UVJ color selection or have $\Delta MS < 0.6$ (~ 1.2 dex below the MS). This way we define as QGs objects that have sufficiently evolved to be treated apart from SFGs.

Secondly, we separated the population of red, dust-obscured SFGs (i.e., RedSFGs) from the blue SFGs (i.e., BlueSFGs) by identifying SFGs particularly faint in the rest-frame UV-to-optical wavelengths. In our redshift range, this intrinsic faintness translates into a faint/extremely faint detection in the optical-to-NIR up to and including the H -band. Previous selection criteria (Wang et al. 2019; Xiao et al. 2023b) were based on HST/WFC3 images in the H -band that were shallower than JWST/NIRCam images in the $F150W$ -band. Here, NIRCam data allow us to go a deeper and study sources that are fainter sources in the observed optical. We therefore decided to adopt:

$$\text{RedSFGs} = \begin{cases} F150W - F444W > 2 \\ F444W < 25 \end{cases}$$

The distribution of our sample in the UVJ diagram in Fig. 4 shows that RedSFGs are located apart from the locus of BlueSFGs and are preferentially found in the dusty star-forming (DSFG) region. In Figure 5, the H -dropout selection criteria of

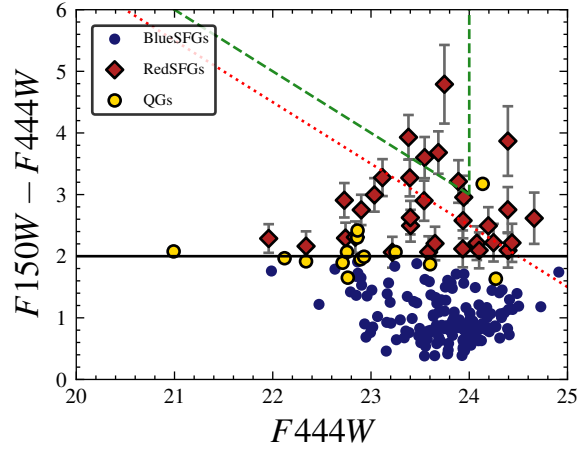


Fig. 5: $F150W - F444W$ versus $F444W$ color-magnitude distribution for our $3 < z < 4$ sample. The markers show the color-selected populations of BlueSFGs, RedSFGs and QGs located above the black solid line defining our RedSFGs selection criteria. As a reference, we indicate the selection criteria for H -dropouts in Wang et al. (2019) (i.e., $F150W > 27$ mag and $F444W < 24$ mag) as a green dashed triangular region and the OFG selection from Xiao et al. (2023b) (i.e., $F150W > 26.5$ mag and $F444W < 25$ mag) as a red dotted line.

Wang et al. (2019) is shown by the green dotted triangular region and the Xiao et al. (2023b) color selection is represented with a red dotted line. The black solid line marks the criteria used in this study. The RedSFGs are shown as red diamonds and lie above this delimiting line. By these criteria, we classified 32 RedSFGs ($\sim 17\%$), 142 BlueSFGs ($\sim 76\%$) and 14 QGs ($\sim 7\%$) in our cleaned mass complete sample of 188 galaxies with $3 < z < 4$ defined in Sect. 3.2.

4. Results

4.1. Integrated Properties

Before studying the resolved properties of BlueSFGs, RedSFGs and QGs, we compared their integrated properties such as their stellar mass, SFR and dust attenuation. In Fig. 6 we show the star-formation MS arising from our mass-complete sample. Here, the SFRs are rescaled to the median redshift of the mass-complete sample: $z_{\text{median}} = 3.49$. This is done by conserving ΔMS for each galaxy relative to the MS associated with their respective redshift. In this way, the rescaled SFRs represent the overall distribution of the sample in the SFR-stellar mass plane. As expected, the majority of color-selected SFGs lie on the MS within the 1σ uncertainty. In particular, we note that RedSFGs also fall on the MS, although, the lack of mid-IR-to-mm data that are necessary to constrain the SFR of highly dusty galaxies (Buat et al. 2019; Figueira et al. 2022), may induce an underestimation of the SFR for some of them. The location of the QGs in the SFR-stellar mass plane, below the main sequence, confirms that the redness of these galaxies is not due to dust attenuation as is the case for RedSFGs, but rather to their old stellar population. This is also illustrated in Fig. 7 where QGs are not as dusty ($A_{\text{v,median}}^{\text{ISM}} \sim 0.8$) as RedSFGs ($A_{\text{v,median}}^{\text{ISM}} \sim 2.2$) despite their similar stellar mass ($\log(M_{\text{*median}}/M_{\odot}) \sim 10.5$). We note here that despite the higher stellar mass of QGs compared to BlueSFGs ($\log(M_{\text{*median}}/M_{\odot}) \sim 9.8$), their dust attenuation does not evolve with mass as it is the case for BlueSFGs

and RedSFGs. They show dust attenuation similar to that of BlueSFGs with $\log(M_*/M_\odot) \sim 10.2$. This low A_V^{ISM} demonstrates that despite being compact and cuspy (see Sect. 4.3), these galaxies have stopped funneling gas and dust in their cores, which would have allowed star-formation to continue. Instead they seem to have reached a physical stability. We also witness a clear offset in dust attenuation between BlueSFGs and RedSFGs, the latter being significantly more attenuated than the first at all stellar masses. Because such a distinction could be due to a bimodal distribution of ellipticities (edge on galaxies tend to be more attenuated than face on's as the column density of dust and gas along the line of sight is greater), we measured the median ellipticity of RedSFGs on the $F444W$ images. We found the median ellipticity of RedSFGs ($e_{\text{median}} = 0.5 \pm 0.17$) to be similar to the one of $\log(M_*/M_\odot) > 10$ typical BlueSFGs ($e_{\text{median}} = 0.52 \pm 0.17$), and no trend was found between their ellipticities and dust-obscuration in both cases. This significantly high dust obscuration in RedSFGs is therefore not due to a geometrical effect.

We have also studied the relative fractions of BlueSFGs, RedSFGs and QGs as a function of stellar mass and indicated them with solid and dotted colored lines in Fig. 8. Here we observe a decrease in the BlueSFGs fraction with increasing stellar mass and an opposite behavior for RedSFGs and QGs that becomes more and more dominant at high mass. At $\log(M_*/M_\odot) > 10.4$, the BlueSFGs fraction drops below 50%, marking the end of their domination. Consequently, QGs and particularly RedSFGs dominate for $\log(M_*/M_\odot) > 10.4$. Above $\log(M_*/M_\odot) > 10.6$, RedSFGs account for over 50% of all galaxies, making them the dominant high-mass population in this redshift range. We note that because of RedSFG incompleteness for $\log(M_*/M_\odot) < 10$, their fractions might be underestimated in this mass regime. Finally, we find that the number density of the RedSFG sample $n \sim 1.1 \times 10^{-4} \text{ Mpc}^{-3}$ is comparable to the one of QG at $z \sim 2$ (McLeod et al. 2021). This is an indication that this population could be the direct progenitor of these QGs found at cosmic noon. In the following, we investigate this RedSFG population and its role in the evolution of SFGs toward quiescence by comparing its resolved properties to those of RedSFGs and QGs.

4.2. Radial Profiles Methodology

To obtain spatially resolved stellar population properties for each galaxy in our mass-complete sample, maintaining a high S/N of typically $S/N > 3$ in the fitted cell was paramount. This is particularly needed for bands probing the Balmer break, essential for reliably measuring dust obscuration. Due to higher dust extinction in RedSFGs compared to BlueSFGs, neither simple pixel-by-pixel binning nor Voronoi binning (Cappellari & Copin 2003) could ensure trustworthy S/N in the UV/optical-bands, resulting in an unfair comparison between the two SFG populations. Consequently, we opted to bin each galaxy into concentric annuli centered on the brightest pixel value in the $F444W$ -band, with a width corresponding to the size of the $F444W$ PSF ($0''.16$ FWHM). Prior to that, we PSF-matched all images to the $F444W$ PSF. We show in Fig. 9 our binning method on RGB, PSF-matched images of a typical BlueSFG, an RedSFG and a QG. This method allowed us to have $S/N > 3$ in each annulus on the $F150W$ images.

We computed the total flux in each of the 10 photometric bands for each annulus by summing the fluxes on a pixel-by-pixel basis. For the total errors in a given annulus and in a given band, we measured total flux within 20 circular apertures in the

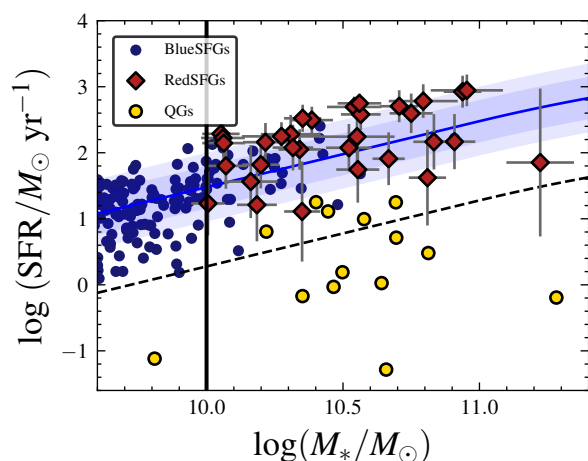


Fig. 6: Location of BlueSFGs, RedSFGs, and QGs at $3 < z < 4$ in the $\text{SFR} - M_*$ plane. The Schreiber et al. (2015) MS is displayed as a solid blue line. We represent the 1σ scatter of this MS associated with $0.5 < \Delta\text{MS} < 2$ (~ 0.3 dex) as a shaded blue area as well as a wider scatter of $0.33 < \Delta\text{MS} < 3$ (~ 0.5 dex) in lighter blue. We rescaled all SFR values to the median redshift of our mass-complete sample ($z_{\text{median}} = 3.51$) as explained in the main text. The sample is mass-complete for the three populations above the thick black line.

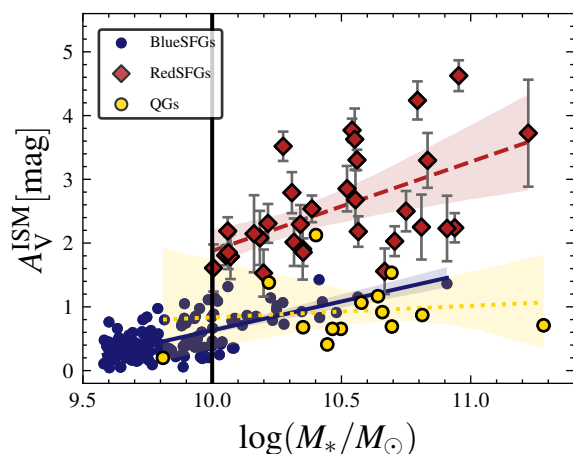


Fig. 7: Dust attenuation as a function of stellar mass for our final $3 < z < 4$ sample. BlueSFGs, RedSFGs and QGs are represented with blue dots, red diamonds and yellow dots with black circle, respectively. Their regression lines and $\sim 95\%$ uncertainties are shown with a solid, dashed and dotted line with a shaded area. We indicate the 99% mass-completeness limit of the sample with a thick black line.

vicinity of the sources that contained the same number of pixels as the annulus under consideration, and calculated the standard deviation of these measured fluxes. The errors were then assumed to be constant for all pixels belonging to an annulus. Finally, we conducted SED-fitting for each annulus using Cigale using the same grid as in Sect. 2.4 and shown in Table 1. We computed the stellar mass density (Σ_*) and the star formation rate density (Σ_{SFR}) by dividing the total mass and SFR in the annulus by the total area within each of them.

Figure 9 shows for each studied sub-population, the best fit output by Cigale for the innermost annulus and the third outer

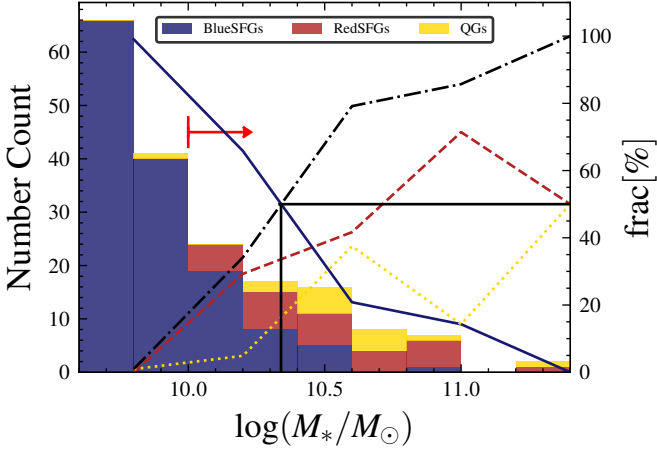


Fig. 8: Mass distribution and relative fractions of the 142 BlueSFGs (blue solid line), 32 RedSFGs (red dashed line) and 14 QGs (yellow dotted line) as a function of stellar mass. The cumulative contribution of RedSFGs and QGs to the total number count as a function of stellar mass is displayed as a black dash-dotted line. The black solid lines show the stellar mass above which $> 50\%$ of galaxies are either RedSFGs or QGs. The arrow recalls the mass completeness limit for the RedSFGs population.

annulus (referred to as annulus 1 and 3, respectively). These images and best fits highlight the peculiarity of RedSFGs as being more compact and redder than BlueSFGs and QGs for a given stellar mass. We also acknowledge the high dust obscuration of RedSFGs that significantly impacts the UV and optical part of their SED.

To compare the profiles of the three populations, which span a wide range of stellar mass and SFR, it is necessary to apply a re-normalization in order to remove any dependence of mass and SFR on radial profiles. For example, it is well-known that SFGs follow a mass-size relation (Kormendy & Bender 1996; Shen et al. 2003; Trujillo et al. 2006; Buitrago et al. 2008; Bruce et al. 2012; Ono et al. 2013; van der Wel et al. 2014; Lange et al. 2015; Allen et al. 2017; Dimauro et al. 2019; Mowla et al. 2019; Nedkova et al. 2021; Ward et al. 2024), with the most massive SFGs being more extended, whereas QGs exhibit a distinct sequence in the mass-size plane (Ward et al. 2024) and RedSFGs may also adhere to a different relation due to their pronounced compactness at higher masses compared to BlueSFGs (Gómez-Guijarro et al. 2023). We took this mass effect into account by rescaling the radii to the median mass of our BlueSFGs sample ($\log(M_{*median}/M_{\odot}) \sim 9.8$) using the Ward et al. (2024) mass-size relation of SFGs. Similarly, we re-scaled the Σ_{*} , Σ_{SFR} and A_{ν}^{ISM} profiles to this same median mass using the Schreiber et al. (2015) MS at $z_{median} = 3.49$ and the $A_{\nu}^{ISM} - \log(M_{*}/M_{\odot})$ linear relation of BlueSFGs shown in Fig. 7. This way, we ensured a fair comparison between these three galaxy populations, allowing us to place the QGs and RedSFGs in the context of BlueSFGs. To compare their morphologies, we computed the median of these re-normalized radial profiles for Σ_{*} , Σ_{SFR} , A_{ν}^{ISM} , sSFR, and mass-weighted age.

4.3. Radial profiles in Σ_{*} , Σ_{SFR} , A_{ν}^{ISM} , sSFR and mass-weighted age

Figure 10 displays the normalized median profiles Σ_{*} , Σ_{SFR} , A_{ν}^{ISM} , sSFR and mass-weighted age inferred by our SED fitting

procedure. The median Σ_{*} profiles of RedSFGs and QGs are almost identical, leading to similar half-mass radii that are about 37% smaller than those of BlueSFGs. The latter show a shallower increase in Σ_{*} towards the center, indicating a more extensive stellar profile. This indicates that the RedSFG population has developed a bulge characteristic of the QG population.

According to the Σ_{SFR} distribution of QGs, they no longer form stars at all radii, which is not the case for BlueSFGs showing a steady decrease towards their outskirts. On the other hand, the SFR profile of RedSFGs is similar in the core to that of BlueSFGs, but shows a steeper gradient, meaning that these galaxies are still in the process of building up their central stellar bulge.

To compare past star formation, measured by Σ_{*} , with current star formation, given by Σ_{SFR} as a function of radius, we measured the sSFR profiles of our galaxies. This gives us indication on ongoing evolution of their structure. The constant sSFR at all radii for BlueSFGs and RedSFGs indicates that the latest will not change much in the future, whereas QGs have suppressed star formation in their cores. Since the Σ_{SFR} profile of the QGs seems to be constant, their sSFR profile reflects the Σ_{*} profile. The median mass-weighted age profiles of RedSFGs and QGs are identical and higher than that of BlueSFGs, which contain a young population at all radii. This indicates that RedSFGs constitute a population of SFGs that have lived long enough to develop an old, massive bulge.

We see an A_{ν}^{ISM} gradient toward the center of the BlueSFGs and RedSFGs indicating an increasing concentration of dust. However, while this gradient is shallow for BlueSFGs, it is really steep for RedSFGs. On the contrary, QGs do not exhibit any A_{ν}^{ISM} radial gradient, and at all radii have A_{ν}^{ISM} value consistent with very little dust/gas content. The lack of star formation in these QGs is thus mostly due to the lack of gas content for their mass rather than a low star formation efficiency. These observations of the A_{ν}^{ISM} profile definitively highlight the particularity of RedSFGs as outliers of the star-forming galaxy population with their high attenuation characterized by their high dust concentration.

To study this apparent bimodality between RedSFGs and BlueSFGs as a function of stellar mass, we characterize the slope of the radial profiles presented in Fig. 10 but grouping galaxies in several stellar mass bins. The slopes of these radial profiles are in this analysis simply approximated by a linear fit of the three innermost annuli, and we named C_{Mass} , C_{SFR} , $C_{A_{\nu}^{ISM}}$, C_{sSFR} and C_{Age} the measured slopes that we interpret as the concentrations of these physical quantities. Figure 11 shows that the concentration of stellar mass increases with galaxy mass for BlueSFGs and RedSFGs while QGs are found to have a constant concentration, although probing a relatively narrow mass range. However, we note that the most massive QG exhibit a slightly lower stellar mass concentration which could be interpreted as a sign of recent mergers, possibly dry mergers, which would not increase the stellar mass concentration in the center as in-situ star formation does, but rather in their outskirts (Naab et al. 2006; Nipoti et al. 2009). The projected surface density of stars in RedSFGs with $\log(M_{*median}/M_{\odot}) > 10.5$ exhibits the same concentration as QGs, both being higher than the one of BlueSFGs. This suggests that if massive RedSFGs stop forming stars they will end up with the same spatial configuration as QGs. Therefore, it confirms the bulge formation of this population and its link to QGs while suggesting that we are indeed witnessing in-situ bulge formation in RedSFGs, which is a pre-requisite to the formation of QGs. In contrast, the most massive BlueSFGs do not show such a concentration of mass, showing that without invoking a violent, ma-

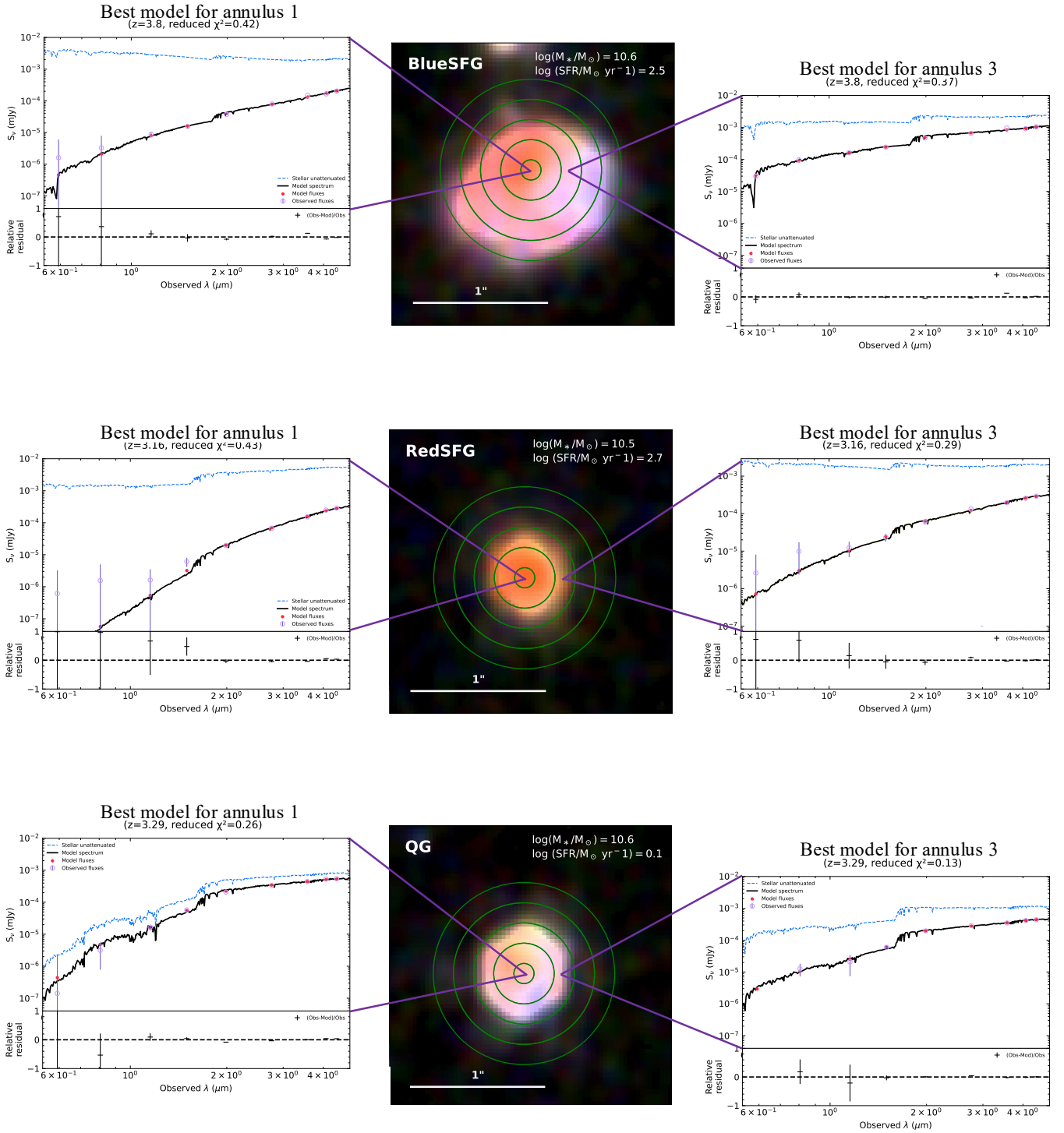


Fig. 9: Illustration of the methodology used to compute radial profiles. From top to bottom, we show an example of BlueSFG, RedSFG and QG RGB cutouts generated using the $F200W$, $F277W$, $F356W$ -bands PSF-matched to the $F444W$ filter. Each cutout has a $2.1'' \times 2.1''$ angular size and contains a $1''$ white bar that defines the scale of the image. For each galaxy, five concentric rings with a constant width equal to the FWHM of the $F444W$ -band are displayed. In addition, for each cutout, we present the best model spectra produced by Cigale for annulus 1 (the innermost) and annulus 3. In those, the blue curve is the unattenuated stellar emission

for merger event, they can not be the progenitors of QGs. However, the dispersion of high-mass BlueSFGs suggests that some SFGs (two in this case) have mass profiles similar to those of RedSFGs and QGs while lacking the A_{ν}^{ISM} concentration characteristic of RedSFGs. Indeed, the bimodality between BlueSFGs

and RedSFGs is very significant when looking at the A_{ν}^{ISM} concentration, with RedSFGs having more concentrated A_{ν}^{ISM} at all masses. This result demonstrates that the BlueSFGs/RedSFGs bimodality is not only linked to stellar mass, but that there is a second-order driver of this bimodality, namely the distribution

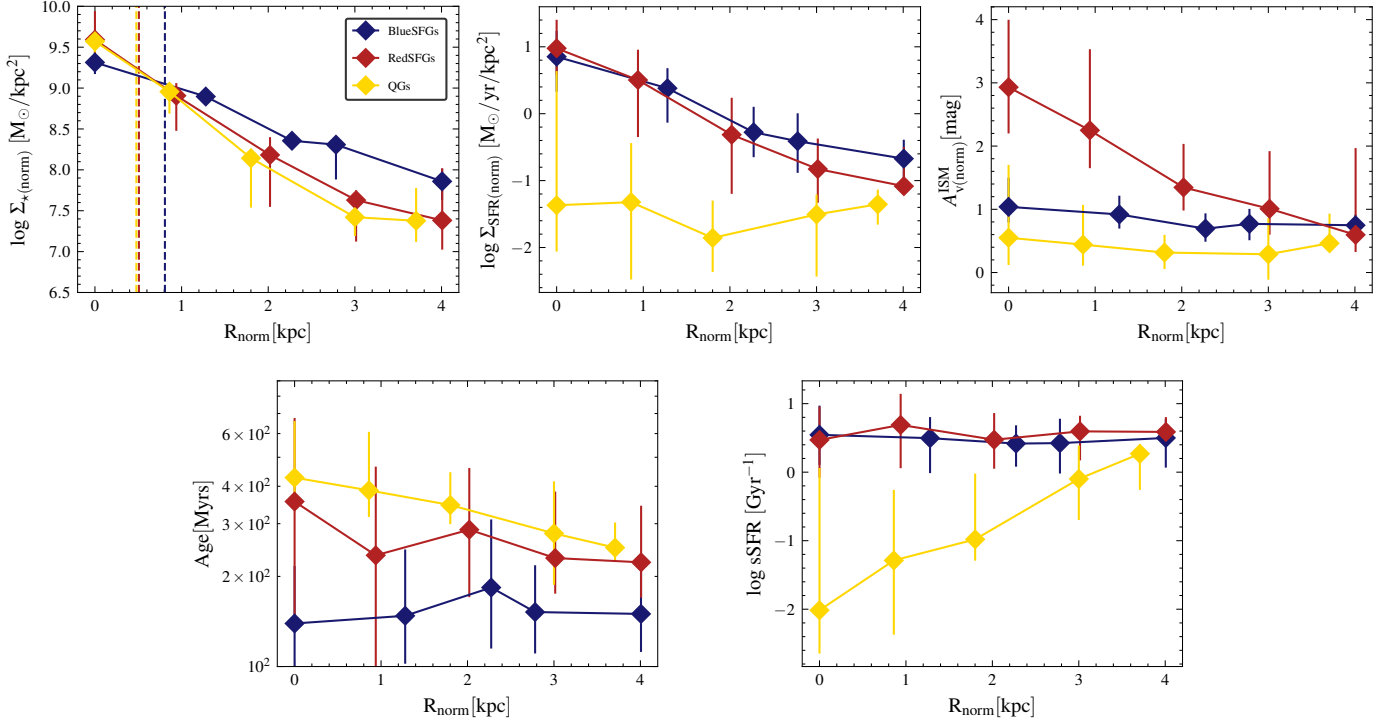


Fig. 10: From left to right and top to bottom, stellar mass density (Σ_\star), star formation rate density (Σ_{SFR}), dust attenuation (A_V^{ISM}), sSFR and mass-weighted age normalized median radial profiles inferred using *Cigale* for BlueSFGs (in blue), RedSFGs (in red) and QGs (in yellow). In the Σ_\star panel we indicate the (normalized) half-mass effective radius for each population with a vertical dashed line.

of dust in galaxies at these redshifts that indicates a compaction event.

We also observe a drop of the SFR, A_V^{ISM} and sSFR concentrations for the most massive RedSFGs, such that their properties reassemble those of QGs. Coupled with the increased mass-weighted age concentration indicating an older stellar population in the core, this suggests that for these massive RedSFGs with highly concentrated stellar component, an inside-out quenching mechanism is at play.

5. Discussion

We find that the sub-population of RedSFGs exhibit steeper radial gradients in stellar mass (Σ_\star), star-formation (Σ_{SFR}) and dust-attenuation (A_V^{ISM}) than their parent population of BlueSFGs. In addition, we observed a similar stellar concentration between RedSFGs and QGs, particularly for RedSFGs with $\log(M_\star/M_\odot) > 10.5$. This indicates that this population has and is still assembling a massive bulge in its core, which is not the case for even the most massive BlueSFGs. This bulge growth is probably closely related to the A_V^{ISM} gradient, which is steeper for RedSFGs at all masses compared to BlueSFGs. If we relate the dust obscuration to the gas content of galaxies, our results suggest that OFGs have undergone a phase of compaction of their gas content, which has been channeled into their cores, producing a high A_V^{ISM} and SFR gradients. This mechanism therefore allows for compact, main-sequence-like star formation in their cores, particularly around $\log(M_\star/M_\odot) \sim 10.5$, where the concentration of A_V^{ISM} is highest, which would lead to efficient consumption of the gas into stars and consequently to quenching.

We further note that the SFR concentration of RedSFGs derived in this study is likely a lower limit of the true Σ_{SFR} of this population. Indeed, while CF00 seems to better recover the true SFR of massive and dusty galaxies (see Sect. 2.4), the lack of resolved FIR data does not allow an accurate determination of the SFR distribution. This could have a particularly high impact at the center of RedSFGs, which is heavily shrouded by dust. The SFR concentration could then be even more pronounced than that observed in this work.

The question of whether or not a compaction phase is necessary to explain the concentration of stellar mass observed in RedSFGs is addressed in Fig. 12. Here, we calculate the evolution of the radial distribution of stars from Σ_{SFR} in each annulus and show that BlueSFGs will not naturally transform into RedSFGs if they maintain their radial Σ_{SFR} profile over the next 300 Myrs (blue dotted curve). Instead, a significant compaction event with a steeper Σ_{SFR} profile is required for BlueSFGs to evolve into RedSFGs (blue dashed curve). The duration of this compaction phase, around 300 Myrs, corresponds to the mass-weighted median age profile observed at the center of the RedSFGs and QG. This suggests that RedSFGs are the result of the evolution of BlueSFGs which experienced a compaction event over a duration of around 300 Myrs.

Figure 11 lower left panel also shows that while most BlueSFGs and RedSFGs do not exhibit any strong radial sSFR gradient (indicating that the stellar structure of these populations will not be modified much by current star formation activity), the most massive RedSFGs break this finding by showing a similar sSFR profile to the QGs. We interpret this population as being depleted of gas at its center (decrease in its A_V^{ISM} concentration)

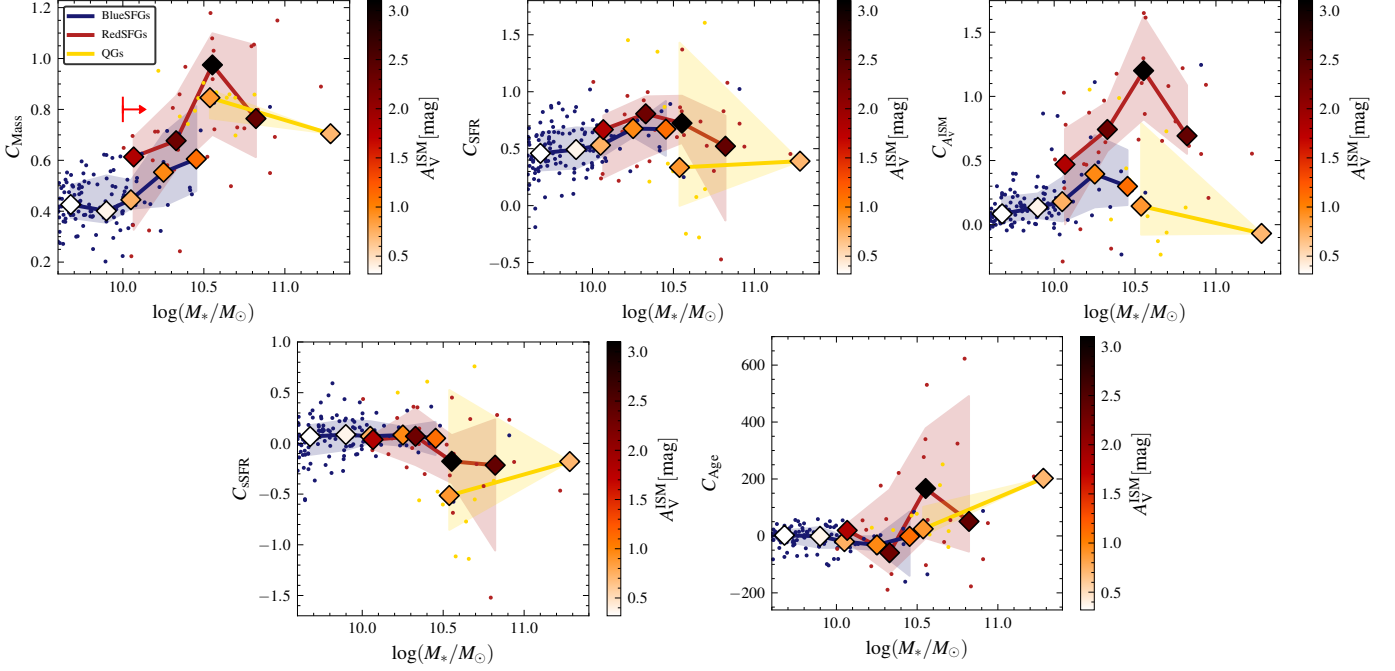


Fig. 11: From left to right and top to bottom, Σ_* , Σ_{SFR} , A_V^{ISM} , sSFR and mass-weighted age concentrations as a function of stellar mass. The different concentrations are determined by measuring the slopes of the three innermost annuli of each curve individually. In each panel, BlueSFGs, RedSFGs and QG are marked by blue, red and yellow dots, respectively. Medians in stellar mass bins are displayed for each population as diamonds, color-coded by the median dust attenuation in the bin. Uncertainties are represented by shaded regions of the color of the represented population. The medians are centered on the median stellar mass of each bin containing at least four galaxies (with the exception of the most massive QG bin, which contains only one galaxy).

while continuing to form stars at its periphery. This leads to a decrease in its stellar mass concentration and converge to that of the QG population.

Finally, the median mass of the RedSFG population ($\log(M_*/M_\odot) \sim 10.5$), together with its dominance above this mass, and our observation that the most massive RedSFGs exhibit a typical QG stellar mass profile, point in the direction of a major compaction event that allows an in-situ growth of a bulge. Some BlueSFGs experienced this compaction event after spending some time on the main sequence and reaching a typical stellar mass of $\log(M_*/M_\odot) \sim 10.5$. This major compaction is assumed to be “wet” according to [Dekel & Burkert \(2014\)](#); [Zolotov et al. \(2015\)](#) so that during this phase, angular momentum loss allows cold gas to be efficiently channeled into galaxy cores, producing MS-type star formation with optically thick dust and ISM enrichment. What triggers such a compaction phase is beyond the scope of this article, but scenarios such as a major merger or consecutive minor mergers ([Dekel & Cox 2006](#); [Covington et al. 2011](#)), counter-rotating cold gas accretion ([Danovich et al. 2015](#)), recycling fountains ([Chabanier et al. 2020](#)) or satellite tidal compression ([Renaud et al. 2014](#)) are advocated by simulations which facilitate efficient in-situ bulge mass growth. The result is a compact mass profile consistent with that of passive galaxies, once all the gas in the galaxies has been depleted and star formation has stopped.

The number density of RedSFGs ($n \sim 1.23 \times 10^{-4} \text{Mpc}^{-3}$) is of the same order of magnitude as the one of QGs at $z \sim 2$ ($n \sim 10^{-4} \text{Mpc}^{-3}$) ([McLeod et al. 2021](#)). This suggests that RedSFGs at $3 < z < 4$ are good candidate for being the progenitor of typical massive QGs at $z \sim 2$ ([McLeod et al. 2021](#)) and is also

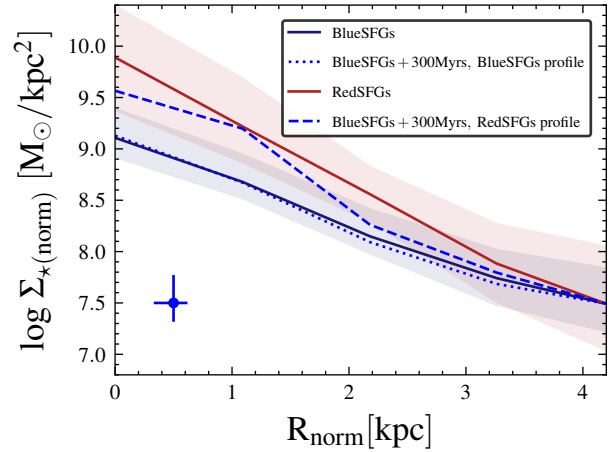


Fig. 12: Median radial profiles of Σ_* for BlueSFGs (in solid blue line) and RedSFGs (in solid red line) with their associated uncertainties represented as blue and shaded regions, respectively. The blue dotted curve represent the radial evolution of Σ_* for BlueSFGs over the next 300 Myrs, derived by applying their median radial profile of star formation surface density (Σ_{SFR}), assumed constant during this period. Additionally, the evolution of the median Σ_* radial profile of BlueSFGs over the next 300 Myrs considering the Σ_{SFR} profile of RedSFGs is displayed as a dashed blue curve. Each profile is normalised to the Σ_* at 4 kpc of RedSFGs. We display the typical median uncertainty of the dotted and dashed profiles by a blue error bar.

consistent with the fact that the bulk of QGs at $z \sim 2$ are compact (van der Wel et al. 2014; van Dokkum et al. 2015).

We also note that the typical stellar mass ($\log(M_*/M_\odot) \sim 10.5$) of RedSFGs corresponds to the critical mass defining the bimodality between BlueSFGs and red QGs in the local Universe (Baldry et al. 2004) and is consistent with the wet compaction scenario advocated in simulations (Behroozi et al. 2013; Dekel et al. 2019). Indeed, the wet compaction phase should occur close to this stellar mass, as it is confined by two main physical mechanisms: supernova feedback and virial shock heating of the circumgalactic medium (CGM). On the one hand, for $M_* < M_{\text{crit}}$, the galaxies' potential well is not deep enough to retain the gas expelled by supernova feedback or to allow a significant portion of the gas to heat up, making them particularly effective at suppressing star formation and consequently stopping the gas compaction. On the other hand, for $M_* > M_{\text{crit}}$, the CGM surrounding the halos is heated by viral shocks that warm the incoming cold gas coming from the intergalactic medium via filaments. The result is a small amount of cold gas, which is not conducive to efficient star formation. It is also suggested that the growth of a super-massive black hole in such a massive system is possible and would guarantee long-term quenching through AGN feedback (Weinberger et al. 2018) once star formation has stopped. According to Pérez-González et al. (2023) and Barufet et al. (2024) it is possible that $\sim 10\%$ of RedSFGs contain a highly obscured AGN.

Overall, this scenario is consistent with our observations of this red population and suggests that RedSFGs can be defined as a phase in galaxy evolution that creates a bimodality between blue and red SFGs. This bimodality in SFGs in place at $z = 3-4$ defines a primeval bimodality that will lead to the formation of today's massive ellipticals.

6. Summary

In this work, we studied the transition from SFGs to QGs by investigating the morphology of a color-selected, massive and dust-obscured population of galaxies, faint in the observed UV/optical but bright in the NIR making them particularly red called RedSFGs in this work. We focused on this population in the context of a mass-complete sample of 188 galaxies at $3 < z < 4$ with $\log(M_*/M_\odot) > 9.6$, cleaned from potential AGN contaminants, point sources, and galaxies with uncertain photometric redshift determination in the JWST/CEERS field.

Among our mass-complete sample, $\sim 17\%$ of the galaxies are classified as red RedSFGs, $\sim 76\%$ are blue BlueSFGs, and $\sim 7\%$ are classified as QGs. We fitted the resolved SED of each galaxy and derived its median Σ_* , Σ_{SFR} , sSFR, A_V^{ISM} and mass-weighted age profiles. Our conclusions can be summarized as follows:

1. RedSFGs and QGs together account for over 50% of galaxies at $\log(M_*/M_\odot) > 10.5$, and this fraction increases with mass. They make up $> 80\%$ at $\log(M_*/M_\odot) \sim 11$ with a large predominance of RedSFGs for $\log(M_*/M_\odot) > 10.6$ where they represent 50% of all galaxies.
2. Radial profiles confirm the compactness of the RedSFGs stellar mass distribution, which is similar to that of the QGs. This suggests that this population is the link in terms of morphological transition between disk-dominated BlueSFGs and bulge-dominated QGs. Their mass-weighted age profile is also similar to that of QGs, confirming that RedSFGs are SFGs on their way to becoming QGs after spending some time on the MS.

3. The Σ_{SFR} and dust attenuation profiles of RedSFGs also show a high concentration and indicate a gas compaction event. These profiles suggest that we are witnessing the massive bulge growth necessary to explain the compact stellar morphology of RedSFGs. In addition, we tested whether BlueSFGs were able to obtain the Σ_* profiles of RedSFGs in less than 300 Myrs by applying the Σ_{SFR} profile of RedSFGs to them. We have found that only the application of RedSFGs Σ_{SFR} profile can produce a Σ_* distribution similar to that of RedSFGs. This reinforces the need for a compaction event happening in-situ to become RedSFGs, and subsequently QGs. This compaction event is then creating a morphological bimodality between BlueSFGs and RedSFGs.
4. We have investigated the evolution with mass of this bimodality and found that dust attenuation, Σ_* and Σ_{SFR} are more concentrated at all masses in RedSFGs, with a peak of these concentrations for $\log(M_*/M_\odot) \sim 10.5$. The fact that the most massive BlueSFGs, which do not show any sign of compaction, do not reach the stellar mass concentration of QGs, proves that increasing stellar mass alone cannot drive a SFGs towards quiescence, and that compaction is required.
5. The most massive RedSFGs in our sample, although showing a highly concentrated bulge, strong dust attenuation and MS-type star formation, also show a significant decrease in Σ_{SFR} , A_V^{ISM} and sSFR concentrations corresponding to suppressed star formation in their cores which contrasts with lower mass RedSFGs. We interpret these deviations from the general mass trends as a sign that these galaxies are in an inside-out quenching process.
6. Our results suggest that the RedSFG population is linked to the critical mass $\log(M_{\text{crit}}/M_\odot) \sim 10.5$ defining the bimodality between QGs and SFGs in the local Universe. This validates the nature of this population as the primeval link between SFGs and QGs.

Our findings can be related to the galaxy evolution scenario suggested in Behroozi et al. (2013), Dekel et al. (2019) by assuming that RedSFGs define a population of SFGs which undergo a compaction phase. They experience the final compaction of their gas content once they reach the critical mass $\log(M_{\text{crit}}/M_\odot) \sim 10.5$, leading to inside-out quenching. This means that the so-called bimodality between local SFGs and QGs originates in a bimodality already existing at $z = 3-4$ between SFGs that have experienced (RedSFGs), or are experiencing, a compaction event and those that have not (BlueSFGs). We suggest that this primeval bimodality takes its seed in relatively rapid compaction events (< 300 Myrs) that lead to a short depletion timescale to transform the gas into stars in a concentrated, dust-shrouded region. The dust channeled into the core and produced by star-formation activity is trapped in the galaxy's gravitational potential, producing a steep A_V^{ISM} gradient characteristic of the RedSFG phase. In order to put better constraints on the dust and gas content in this obscured population, deep and high-resolution imaging with ALMA would be necessary. Combined with multi-wavelength photometry, especially with MIRI, this would allow better stellar mass estimates of these obscured system and shed light on the possible AGN contribution in their cores. Spatially resolved spectroscopy could also be of interest to study the metallicity and age gradients as well as resolved SFH and velocity profiles of these galaxies. In particular, studies of the kinematic of RedSFG would allow to measure their three-dimensional stellar distribution and explore their triaxial properties. This three-dimensional information is vital to test and confirm the in-situ bulge formation scenario that we are highlighting

in this work. Putting all this together, we will be able to lift the veil on the physical process underlying the major compaction phase in the early universe.

Acknowledgements. MT acknowledges support from CNES. This work was supported by the Programme National Cosmology et Galaxies (PNCG) of CNRS/INSU with INP and IN2P3, co-funded by CEA and CNES. MT acknowledges the following open sources softwares used in this work : *Numpy* (Harris et al. 2020), *Astropy* (Astropy Collaboration et al. 2013, 2018, 2022), *Photutils* (Bradley et al. 2024) and *SciencePlots* (Garrett et al. 2023).

References

- Alcalde Pampliega, B., Pérez-González, P. G., Barro, G., et al. 2019, *The Astrophysical Journal*, 876, L135
- Allen, R. J., Kacprzak, G. G., Glazebrook, K., et al. 2017, *The Astrophysical Journal Letters*, 834, L11
- Arnouts, S., Cristiani, S., Moscardini, L., et al. 1999, *Monthly Notices of the Royal Astronomical Society*, 310, 540
- Arrabal Haro, P., Rodríguez Espinosa, J. M., Muñoz-Tuñón, C., et al. 2020, *Monthly Notices of the Royal Astronomical Society*, 495, 1807
- Astropy Collaboration, Price-Whelan, A. M., Lim, P. L., et al. 2022, *The Astrophysical Journal*, 935, 167
- Astropy Collaboration, Price-Whelan, A. M., Sipőcz, B. M., et al. 2018, *The Astronomical Journal*, 156, 123
- Astropy Collaboration, Robitaille, T. P., Tollerud, E. J., et al. 2013, *Astronomy and Astrophysics*, 558, A33
- Bagley, M. B., Finkelstein, S. L., Koekemoer, A. M., et al. 2023, *The Astrophysical Journal*, 946, L12
- Baldry, I. K., Glazebrook, K., Brinkmann, J., et al. 2004, *The Astrophysical Journal*, 600, 681
- Barrufet, L., Oesch, P., Marques-Chaves, R., et al. 2024, *Quiescent or Dusty? Unveiling the Nature of Extremely Red Galaxies at $z > 3$*
- Barrufet, L., Oesch, P. A., Weibel, A., et al. 2023, *Monthly Notices of the Royal Astronomical Society*, 522, 449
- Behroozi, P. S., Wechsler, R. H., & Conroy, C. 2013, *The Astrophysical Journal*, 770, 57
- Bell, E. F. 2003, *The Astrophysical Journal*, 586, 794
- Bertin, E. & Arnouts, S. 1996, *Astronomy and Astrophysics Supplement Series*, 117, 393
- Bolzonella, M., Miralles, J. M., & Pelló, R. 2000, *Astronomy and Astrophysics*, 363, 476
- Boquien, M., Burgarella, D., Roehlly, Y., et al. 2019, *Astronomy & Astrophysics*, 622, A103
- Bradley, L., Sipőcz, B., Robitaille, T., et al. 2024, *Astropy/Photutils: 1.12.0, Zenodo*
- Brammer, G. B., van Dokkum, P. G., & Coppi, P. 2008, *The Astrophysical Journal*, 686, 1503
- Brammer, G. B., Whitaker, K. E., van Dokkum, P. G., et al. 2011, *The Astrophysical Journal*, 739, 24
- Bruce, V. A., Dunlop, J. S., Cirasuolo, M., et al. 2012, *Monthly Notices of the Royal Astronomical Society*, 427, 1666
- Bruzual, G. & Charlot, S. 2003, *Monthly Notices of the Royal Astronomical Society*, 344, 1000
- Buat, V., Ciesla, L., Boquien, M., Malek, K., & Burgarella, D. 2019, *Astronomy & Astrophysics*, 632, A79
- Buat, V., Noll, S., Burgarella, D., et al. 2012, *Astronomy & Astrophysics*, 545, A141
- Buitrago, F., Trujillo, I., Conselice, C. J., et al. 2008, *The Astrophysical Journal*, 687, L61
- Bunker, A. J., Cameron, A. J., Curtis-Lake, E., et al. 2024, *Astronomy & Astrophysics*
- Calabro, A., Pentericci, L., Santini, P., et al. 2024, *Astronomy & Astrophysics*
- Calzetti, D., Armus, L., Bohlin, R. C., et al. 2000, *The Astrophysical Journal*, 533, 682
- Cappellari, M. & Copin, Y. 2003, *Monthly Notices of the Royal Astronomical Society*, 342, 345
- Caputi, K. I., Dunlop, J. S., McLure, R. J., et al. 2012, *The Astrophysical Journal*, 750, L20
- Carnall, A. C., McLeod, D. J., McLure, R. J., et al. 2023a, *Monthly Notices of the Royal Astronomical Society*, 520, 3974
- Carnall, A. C., McLure, R. J., Dunlop, J. S., et al. 2023b, *Nature*, 619, 716
- Chabanier, S., Bournaud, F., Dubois, Y., et al. 2020, *Astronomy & Astrophysics*, 643, L8
- Chabrier, G. 2003, *Publications of the Astronomical Society of the Pacific*, 115, 763
- Charlot, S. & Fall, S. M. 2000, *The Astrophysical Journal*, 539, 718
- Chevallard, J. & Charlot, S. 2016, *Monthly Notices of the Royal Astronomical Society*, 462, 1415
- Ciesla, L., Elbaz, D., Ilbert, O., et al. 2024, *Astronomy and Astrophysics*, 686, A128
- Conroy, C. & Gunn, J. E. 2010, *The Astrophysical Journal*, 712, 833
- Conselice, C. J., Basham, J. T. F., Bettaney, D. O., et al. 2024, *Monthly Notices of the Royal Astronomical Society*, 531, 4857
- Covington, M. D., Primack, J. R., Porter, L. A., et al. 2011, *Monthly Notices of the Royal Astronomical Society*, 415, 3135
- Daddi, E., Dickinson, M., Morrison, G., et al. 2007, *The Astrophysical Journal*, 670, 156
- Danovich, M., Dekel, A., Hahn, O., Ceverino, D., & Primack, J. 2015, *Monthly Notices of the Royal Astronomical Society*, 449, 2087
- Davis, M., Guhathakurta, P., Konidaris, N. P., et al. 2007, *The Astrophysical Journal*, 660, L1
- de Barros, S., Schaerer, D., & Stark, D. P. 2014, *Astronomy and Astrophysics*, 563, A81
- Dekel, A. & Burkert, A. 2014, *Monthly Notices of the Royal Astronomical Society*, 438, 1870
- Dekel, A. & Cox, T. J. 2006, *Monthly Notices of the Royal Astronomical Society*, 370, 1445
- Dekel, A., Lapiner, S., & Dubois, Y. 2019, *Origin of the Golden Mass of Galaxies and Black Holes*
- Delhaize, J., Smolčić, V., Delvecchio, I., et al. 2017, *Astronomy & Astrophysics*, 602, A4
- Delvecchio, I., Smolčić, V., Zamorani, G., et al. 2017, *Astronomy & Astrophysics*, 602, A3
- D'Eugenio, F., Maiolino, R., Carniani, S., et al. 2024, *Astronomy & Astrophysics*, 689, A152
- Dickinson, M., Giavalisco, M., & GOODS Team. 2003, *The Great Observatories Origins Deep Survey* (eprint: arXiv:astro-ph/0204213), 324
- Dimauro, P., Huertas-Company, M., Daddi, E., et al. 2019, *Monthly Notices of the Royal Astronomical Society*, 489, 4135
- Eisenstein, D. J., Johnson, B. D., Robertson, B., et al. 2023a, *The JADES Origins Field: A New JWST Deep Field in the JADES Second NIRC2 Data Release*
- Eisenstein, D. J., Willott, C., Alberts, S., et al. 2023b, *Overview of the JWST Advanced Deep Extragalactic Survey (JADES)*
- Elbaz, D., Daddi, E., Le Borgne, D., et al. 2007, *Astronomy and Astrophysics*, 468, 33
- Fang, J. J., Faber, S. M., Koo, D. C., et al. 2018, *The Astrophysical Journal*, 858, 100
- Figueira, M., Pollo, A., Malek, K., et al. 2022, *Astronomy & Astrophysics*, 667, A29
- Finkelstein, S. L., Bagley, M. B., Arrabal Haro, P., et al. 2022, *The Astrophysical Journal*, 940, L55
- Finkelstein, S. L., Dickinson, M., Ferguson, H. C., et al. 2017, *JWST Proposal ID 1345. Cycle 0 Early Release Science*, 1345
- Finkelstein, S. L., Leung, G. C. K., Bagley, M. B., et al. 2024, *The Astrophysical Journal*, 969, L2
- Franco, M., Elbaz, D., Béthermin, M., et al. 2018, *Astronomy & Astrophysics*, 620, A152
- Fumagalli, M., Labbé, I., Patel, S. G., et al. 2014, *The Astrophysical Journal*, 796, 35
- Gaia Collaboration, Brown, A. G. A., Vallenari, A., et al. 2021, *Astronomy and Astrophysics*, 649, A1
- Gardner, J. P., Mather, J. C., Abbott, R., et al. 2023, *Publications of the Astronomical Society of the Pacific*, 135, 068001
- Gardner, J. P., Mather, J. C., Clampin, M., et al. 2006, *Space Science Reviews*, 123, 485
- Garrett, J., Luis, E., H. -H. Peng, et al. 2023, *Garrettj403/SciencePlots: 2.1.1, Zenodo*
- Gawiser, E. 2009, *New Astronomy Reviews*, 53, 50
- Giavalisco, M., Dickinson, M., Ferguson, H. C., et al. 2004a, *The Astrophysical Journal*, 600, L103
- Giavalisco, M., Ferguson, H. C., Koekemoer, A. M., et al. 2004b, *The Astrophysical Journal*, 600, L93
- Gómez-Guijarro, C., Elbaz, D., Xiao, M., et al. 2022, *Astronomy & Astrophysics*, 658, A43
- Gómez-Guijarro, C., Magnelli, B., Elbaz, D., et al. 2023, *Astronomy & Astrophysics*, 677, A34
- Gottumukkala, R., Barrufet, L., Oesch, P. A., et al. 2024, *Monthly Notices of the Royal Astronomical Society*, 530, 966
- Grogin, N. A., Kocevski, D. D., Faber, S. M., et al. 2011, *The Astrophysical Journal Supplement Series*, 197, 35
- Grupponi, C., Béthermin, M., Loiacono, F., et al. 2020, *Astronomy & Astrophysics*, 643, A8
- Hainline, K. N., Johnson, B. D., Robertson, B., et al. 2024, *The Astrophysical Journal*, 964, 71
- Harris, C. R., Millman, K. J., van der Walt, S. J., et al. 2020, *Nature*, 585, 357

- Helou, G., Soifer, B. T., & Rowan-Robinson, M. 1985, *The Astrophysical Journal*, 298, L7
- Huertas-Company, M., Iyer, K. G., Angeloudi, E., et al. 2024, *Astronomy and Astrophysics*, 685, A48
- Ilbert, O., Arnouts, S., McCracken, H. J., et al. 2006, *Astronomy and Astrophysics*, 457, 841
- Jin, S., Daddi, E., Liu, D., et al. 2018, *The Astrophysical Journal*, 864, 56
- Kartaltepe, J. S., Rose, C., Vanderhoof, B. N., et al. 2023, *The Astrophysical Journal Letters*, 946, L15
- Kennicutt, Jr., R. C. 1998, *The Astrophysical Journal*, 498, 541
- Kocevski, D. D., Barro, G., McGrath, E. J., et al. 2023a, *The Astrophysical Journal Letters*, 946, L14
- Kocevski, D. D., Finkelstein, S. L., Barro, G., et al. 2024, *The Rise of Faint, Red AGN at $z > 4.5$: A Sample of Little Red Dots in the JWST Extragalactic Legacy Fields*
- Kocevski, D. D., Onoue, M., Inayoshi, K., et al. 2023b, *The Astrophysical Journal*, 954, L4
- Koekemoer, A. M., Faber, S. M., Ferguson, H. C., et al. 2011, *The Astrophysical Journal Supplement Series*, 197, 36
- Kokorev, V., Brammer, G., Fujimoto, S., et al. 2022, *The Astrophysical Journal Supplement Series*, 263, 38
- Kokorev, V., Caputi, K. I., Greene, J. E., et al. 2024, *The Astrophysical Journal*, 968, 38
- Kormendy, J. & Bender, R. 1996, *The Astrophysical Journal*, 464, L119
- Kriek, M., Shapley, A. E., Reddy, N. A., et al. 2015, *The Astrophysical Journal Supplement Series*, 218, 15
- Labbe, I., Greene, J. E., Bezanson, R., et al. 2023, *UNCOVER: Candidate Red Active Galactic Nuclei at $z < 3$*
- Lange, R., Driver, S. P., Robotham, A. S. G., et al. 2015, *Monthly Notices of the Royal Astronomical Society*, 447, 2603
- Lee, B., Giavalisco, M., Williams, C. C., et al. 2013, *The Astrophysical Journal*, 774, 47
- Liu, C., Hao, L., Wang, H., & Yang, X. 2019, *The Astrophysical Journal*, 878, 69
- Liu, D., Daddi, E., Dickinson, M., et al. 2018, *The Astrophysical Journal*, 853, 172
- Lower, S., Narayanan, D., Leja, J., et al. 2020, *The Astrophysical Journal*, 904, 33
- Luo, B., Brandt, W. N., Xue, Y. Q., et al. 2016, *The Astrophysical Journal Supplement Series*, 228, 2
- Ma, X., Hopkins, P. F., Faucher-Giguère, C.-A., et al. 2016, *Monthly Notices of the Royal Astronomical Society*, 456, 2140
- Magnelli, B., Ivison, R. J., Lutz, D., et al. 2015, *Astronomy & Astrophysics*, 573, A45
- McLeod, D. J., McLure, R. J., Dunlop, J. S., et al. 2021, *Monthly Notices of the Royal Astronomical Society*, 503, 4413
- Mowla, L. A., van Dokkum, P., Brammer, G. B., et al. 2019, *The Astrophysical Journal*, 880, 57
- Muzzin, A., Marchesini, D., Stefanon, M., et al. 2013, *The Astrophysical Journal*, 777, 18
- Naab, T., Khochfar, S., & Burkert, A. 2006, *The Astrophysical Journal*, 636, L81
- Narayanan, D., Lower, S., Torrey, P., et al. 2024, *The Astrophysical Journal*, 961, 73
- Nedkova, K. V., Häußler, B., Marchesini, D., et al. 2021, *Monthly Notices of the Royal Astronomical Society*, 506, 928
- Nelson, E. J., Suess, K. A., Bezanson, R., et al. 2023, *The Astrophysical Journal*, 948, L18
- Nipoti, C., Treu, T., & Bolton, A. S. 2009, *The Astrophysical Journal*, 703, 1531
- Noeske, K. G., Weiner, B. J., Faber, S. M., et al. 2007, *The Astrophysical Journal*, 660, L43
- Oke, J. B. & Gunn, J. E. 1983, *The Astrophysical Journal*, 266, 713
- Ono, Y., Ouchi, M., Curtis-Lake, E., et al. 2013, *The Astrophysical Journal*, 777, 155
- Osborne, C., Salim, S., Damjanov, I., et al. 2020, *The Astrophysical Journal*, 902, 77
- Pacifici, C., Iyer, K. G., Mobasher, B., et al. 2023, *The Astrophysical Journal*, 944, 141
- Patel, S. G., Holden, B. P., Kelson, D. D., et al. 2012, *The Astrophysical Journal*, 748, L27
- Pérez-González, P. G., Barro, G., Annunziatella, M., et al. 2023, *The Astrophysical Journal Letters*, 946, L16
- Popesso, P., Concas, A., Cresci, G., et al. 2023, *Monthly Notices of the Royal Astronomical Society*, 519, 1526
- Renaud, F., Bournaud, F., Kraljic, K., & Duc, P. A. 2014, *Monthly Notices of the Royal Astronomical Society*, 442, L33
- Rieke, M. J., Robertson, B., Tacchella, S., et al. 2023, *The Astrophysical Journal Supplement Series*, 269, 16
- Schreiber, C., Pannella, M., Elbaz, D., et al. 2015, *Astronomy & Astrophysics*, 575, A74
- Seillé, L.-M., Buat, V., Haddad, W., et al. 2022, *Astronomy & Astrophysics*, 665, A137
- Shen, S., Mo, H. J., White, S. D. M., et al. 2003, *Monthly Notices of the Royal Astronomical Society*, 343, 978
- Smail, I., Dudzevičiūtė, U., Gurwell, M., et al. 2023, *The Astrophysical Journal*, 958, 36
- Stefanon, M., Yan, H., Mobasher, B., et al. 2017, *The Astrophysical Journal Supplement Series*, 229, 32
- Sun, F., Helton, J. M., Egami, E., et al. 2024, *The Astrophysical Journal*, 961, 69
- Trujillo, I., Schreiber, N. M. F., Rudnick, G., et al. 2006, *The Astrophysical Journal*, 650, 18
- Valentino, F., Brammer, G., Gould, K. M. L., et al. 2023, *The Astrophysical Journal*, 947, 20
- Valentino, F., Tanaka, M., Davidzon, I., et al. 2020, *The Astrophysical Journal*, 889, 93
- van der Wel, A., Franx, M., van Dokkum, P. G., et al. 2014, *The Astrophysical Journal*, 788, 28
- van Dokkum, P. G., Nelson, E. J., Franx, M., et al. 2015, *The Astrophysical Journal*, 813, 23
- Wang, T., Elbaz, D., Schreiber, C., et al. 2016, *The Astrophysical Journal*, 816, 84
- Wang, T., Schreiber, C., Elbaz, D., et al. 2019, *Nature*, 572, 211
- Wang, W., Yuan, Z., Yu, H., & Mao, J. 2023, *Constraints on the Cosmic Star Formation History via a New Modeling of the SFG Radio Luminosity Function*
- Ward, E., De La Vega, A., Mobasher, B., et al. 2024, *The Astrophysical Journal*, 962, 176
- Weaver, J. R., Davidzon, I., Toft, S., et al. 2023, *Astronomy & Astrophysics*, 677, A184
- Weibel, A., Oesch, P. A., Barrufet, L., et al. 2024, *Monthly Notices of the Royal Astronomical Society*, 533, 1808
- Weinberger, R., Springel, V., Pakmor, R., et al. 2018, *Monthly Notices of the Royal Astronomical Society*, 479, 4056
- Whitaker, K. E., Labbé, I., van Dokkum, P. G., et al. 2011, *The Astrophysical Journal*, 735, 86
- Williams, C. C., Labbe, I., Spilker, J., et al. 2019, *The Astrophysical Journal*, 884, 154
- Williams, R. J., Quadri, R. F., Franx, M., van Dokkum, P., & Labbé, I. 2009, *The Astrophysical Journal*, 691, 1879
- Wuyts, S., Förster Schreiber, N. M., van der Wel, A., et al. 2011, *The Astrophysical Journal*, 742, 96
- Xiao, M., Oesch, P., Elbaz, D., et al. 2023a, *Massive Optically Dark Galaxies Unveiled by JWST Challenge Galaxy Formation Models*
- Xiao, M.-Y., Elbaz, D., Gómez-Guijarro, C., et al. 2023b, *Astronomy & Astrophysics*, 672, A18
- Yamaguchi, Y., Kohno, K., Hatsukade, B., et al. 2019, *The Astrophysical Journal*, 878, 73
- Yuan, F.-T., Burgarella, D., Corre, D., et al. 2019, *Astronomy & Astrophysics*, 631, A123
- Yun, M. S., Reddy, N. A., & Condon, J. J. 2001, *The Astrophysical Journal*, 554, 803
- Zolotov, A., Dekel, A., Mandelker, N., et al. 2015, *Monthly Notices of the Royal Astronomical Society*, 450, 2327

¹ Université Paris-Saclay, Université Paris Cité, CEA, CNRS, AIM, 91191, Gif-sur-Yvette, France

² NSF's National Optical-Infrared Astronomy Research Laboratory, 950 N. Cherry Ave., Tucson, AZ 85719, USA

³ Department of Physics, University of California, Merced, 5200 Lake Road, Merced, CA 92543, USA

⁴ The University of Texas at Austin, 2515 Speedway Blvd Stop C1400, Austin, TX 78712, USA

⁵ European Space Agency (ESA), European Space Astronomy Centre (ESAC), Camino Bajo del Castillo s/n, 28692 Villanueva de la Cañada, Madrid, Spain

⁶ University of Massachusetts Amherst, 710 North Pleasant Street, Amherst, MA 01003-9305, USA

⁷ INAF Osservatorio Astronomico di Roma, Via Frascati 33, 00078 Monteporzio Catone, Rome, Italy

⁸ Dipartimento di Fisica e Astronomia "G. Galilei", Università di Padova, Via Marzolo 8, I-35131 Padova, Italy

⁹ INAF-Osservatorio Astronomico di Padova, Vicolo dell'Osservatorio 5, I-35122, Padova, Italy

¹⁰ Space Telescope Science Institute (STSCI), 3700 San Martin Dr., Baltimore, 21218 MD, USA

- ¹¹ École Polytechnique Fédérale de Lausanne (EPFL), Observatoire de Sauverny, Chemin Pegasi 51, CH-1290 Versoix, Switzerland
- ¹² INAF Astronomical Observatory of Trieste, via G.B. Tiepolo 11, I-34143 Trieste, Italy
- ¹³ Department of Physics and Astronomy, University of Louisville, Natural Science Building 102, 40292 KY, Louisville, USA
- ¹⁴ Aix Marseille Univ, CNRS, CNES, LAM, Marseille, France
- ¹⁵ Astronomy Centre, University of Sussex, Falmer, Brighton BN1 9QH, UK
- ¹⁶ Institute of Space Sciences and Astronomy, University of Malta, Msida, MSD 2080, Malta